JOURNAL OF MATERIALS SCIENCE **38** (2003) 4611–4637

Ceramics for chemical sensing

C. O. PARK
Department of Materials Science and Engineering, KAIST, Taejon 305-701, Korea

S. A. AKBAR
Department of Materials Science and Engineering, CISM, 291 Watts Hall, Ohio State University, Columbus, OH 43210, USA
E-mail: Akbar@mse.eng.ohio-state.edu

Many types of sensors have been developed to detect chemical species in the gas phase. These include optical based on color change or fluoresence, surface acoustic wave (SAW) devices, electrochemical, chemoresistive/semiconductive, field effect transistors (FET), metal-insulator-semiconductor (MIS) diode devices, and many other. Among these, resistive type sensors based on ceramic oxides are particularly attractive because of their low cost, wide range of applications and potential for use in electronic nose. This article focuses mainly on the resistive/semiconductive, especially the surface conductive ceramic oxide type gas sensors. The main emphasis is on the basic principles involving gas-solid reactions. Also discussed are selected applications with an emphasis on sensor design issues. Since SnO_2 can be used as a model system for oxide-based sensors, most of the discussions focuses on this system, though other systems are occasionally highlighted illustrating recent developments.

1. Introduction

There is a continuing need for the development of rugged and reliable chemical sensors capable of making measurements in harsh industrial environments as well as for public health and security [1–7]. The use of chemical sensors covers a wide range of industries such as steelmaking, heat treating, metal casting, glass, ceramic, pulp and paper, automotive, aerospace, utility and power. Emissions monitoring sensors for these applications include those for CO, NO_x, O_2, CO_2, hydrocarbons (HCs) and volatile organic compounds (VOCs). The application of sensor and measurement technology has resulted in many benefits including improved energy efficiency in combustion and chemical processes, better quality and lower scrap or off-specification products, and reduced emissions. Chemical sensors are also being applied in domestic appliances and air quality monitoring. Lately, chemical sensors are attracting attention for applications such as early detection of smoke/fire as well as hazardous chemical agents to provide safety and security in public places and mass transportation systems. According to a recent market report, US demand alone for chemical sensors (gas sensors and biosensors) is projected to reach $2.7 billion by 2006 [8]. For commercial success, major advances in these sensors are required in terms of simple structure, lower cost, selectivity, durability and reliability.

Many types of gas sensors have been developed to detect chemical species in the gas phase. For instance, optical sensors detect gases based on a color change or fluoresence of a probed molecule [9]. Physical sensors, such as Surface Acoustic Wave Devices and Quartz Crystal Microbalances, become chemical sensors when coated with polymers, self-assembled monolayers or other chemically selective materials. Finally, numerous electrical sensors show an electrical response (resistance change, change of electromotive force, etc.) to a chemical change. Field effect transistors (FET) [10], metal-insulator-semiconductor (MIS) diode devices [11, 12], metal oxide semiconductor capacitors [13] and ferroelectric-based devices [14] have been studied for gas sensing. This paper focuses on a group of electrical sensors, which is particularly attractive for the detection of reducing gases in air because they can be made from oxide ceramics. The emphasis will mainly be on the semiconductive (especially surface conductive ceramic oxide) type gas sensors. A separate paper is being devoted to those based on ceramic electrolytes (i.e., potentiometric and amperometric types). Since SnO_2 can be used as a model system for oxide-based sensors, most of the discussions will focus on this system, though other systems will be occasionally highlighted illustrating recent developments.

2. Types of ceramic oxide gas sensors

The most suitable sensors of these types are semiconductor gas sensors using metal oxides. In contrast to other semiconductors that undergo irreversible chemical reactions forming stable oxides upon exposure to air at high temperature, metal oxides remain stable while interacting with oxygen at their surfaces. Gas molecules in the ambient can interact with: (1) bulk grains, (2) electrode/oxide interface and (3) intergranular contacts. These interfacial reactions involving a transfer of electrons bring about a change in the electrical resistance of the material. Hence, these sensors

can be grouped under three distinct categories based on the physical origin responsible for the electrical response:

(a) bulk-conduction based sensor
(b) metal/oxide (electrode/oxide) junction controlled sensor
(c) surface-layer conductive (intergranular controlled) sensor

2.1. Bulk-conduction based sensors

When the defect species in the ceramic have high mobility, or the temperature is high enough, the bulk phase can maintain its stoichiometry in equilibrium with the gas species in the surrounding atmosphere. Because the non-stoichiometric oxide usually exhibits electron or hole conductivity which is dependent on its composition in the gas phase, the concentration of the gas species can be determined by measuring the bulk conductivity of the semiconductive oxide. For instance, the relationship between oxygen partial pressure and the electrical conductivity of a bulk-conduction-based sensor may be represented by

$$\sigma = \sigma_o \exp\left(-\frac{E_a}{kT}\right) P_{O_2}^{\pm\frac{1}{n}} \quad (1)$$

where σ_o, E_a and n are a constant, the activation energy for conduction and a stoichiometric constant determined by the type of dominant bulk defect involved in the equilibrium process between oxygen and the sensor material. A positive dependence $(+1/n)$ is usually observed at high oxygen pressures in the hole-conduction region whereas a negative dependence $(-1/n)$ occurs at low oxygen pressures in the electron-conduction region, as shown in Fig. 1. Hence the change in the bulk conductivity is a reflection of the equilibration between the oxygen activity in the oxide and the oxygen content (P_{O_2}) in the surrounding atmosphere. Sensors based on TiO_2, $BaTiO_3$, CeO_2 and Nb_2O_5 fall under this category [15–18].

According to Equation 1, lower values of n and E_a, respectively, offer a greater sensitivity to changes in the oxygen pressure and lower interference to the temperature fluctuation of the sensor. In oxides with a perovskite-structure, the temperature dependence of conductivity is often considerably less at high oxygen pressure (p-type) than at the low oxygen pressure (n-type), as noticed in Fig. 1. The oxygen deficiency due to the loss of oxygen with rising temperature, contributes to a decrease in conductivity in the p-type range, but supports the conductivity increase from the thermal generation of the electron defects [19]. By doping the oxide with proper solutes, the two effects can cancel and a near zero activation energy can be obtained for both hole and electron conduction. Moseley [20] found a family of doped perovskite-structure ferrites that exhibit almost zero activation energy over a considerable temperature range. The characteristics of TiO_2 and $BaFe_{0.8}Ta_{0.2}O_3$ are listed in Table I.

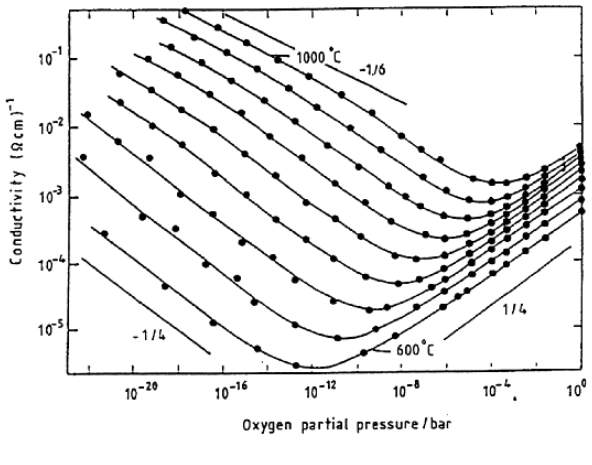

Figure 1 The change in conductivity of $BaTiO_3$ with oxygen pressure at temperature from 600 to 1000°C (50°C intervals) (after ref. 18).

TABLE I Comparison of the oxygen pressure dependence of $BaFe_{0.8}Ta_{0.2}O_3$ with that of TiO_2 [20]

Materials	n	E_a (eV)	Structure	Ref.
TiO_2	−4, −6	1.5	Rutile	[15, 16]
$BaFe_{0.8}Ta_{0.2}O_3$	+5	≈0	Perovskite	[20]

2.2. Metal/oxide junction controlled sensors

The relative work function change upon adsorption of gas species at the metal-oxide interface can give rise to a change in the:

(1) resistance (Schottky barrier diode)
(2) flat band voltage (MOS/MISFET devices)

In a Schottky barrier diode sensor [21], one of the electrode/semiconductor contacts acts as a Schottky barrier (e.g., Pd/SnO_2, Pt/TiO_2) with the other as an ohmic contact. The I–V characteristics of a Schottky diode are described by the thermo-electronic emission as

$$I = A^* T^2 \exp(-V_S/kT)[\exp(eV/nkT) - 1] \quad (2)$$

where A^*, V_S and V, are the Richardson constant, the Schottky barrier height and the bias voltage, respectively. The barrier height (V_S) at the metal electrode/semiconductor interface can vary with the occupation of the surface states at the three-phase boundary (electrode/oxide/gas), which responds to chemisorption of oxidizing and reducing gases such as O_2 and CO. The change in V_S leads to a change in the magnitude of the reverse saturation current and a displacement of the I–V curve at forward bias. Hence the partial-pressure-dependent variation of the interface resistance can be obtained from Fig. 2 for the operation mode of constant voltage or constant current.

The work function change of Pd upon hydrogen adsorption has been known for more than 30 years [22]. In MOS/MISFET (metal-oxide-semiconductor or metal-insulator-semicondcutor field effect transistor) sensors, an oxide/metal (Pd) contact is placed on Si. The work function change is measured with gas adsorption

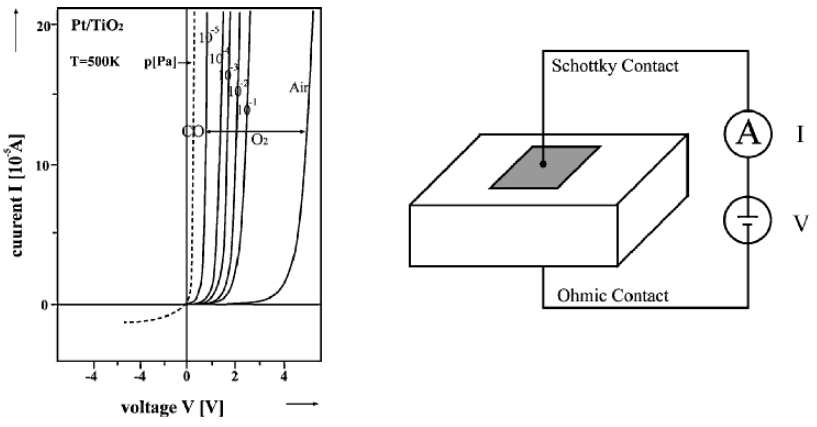

Figure 2 I–V characteristics of Pt/TiO_2 Schottky diode in the presence of CO and O_2 [after ref. 21].

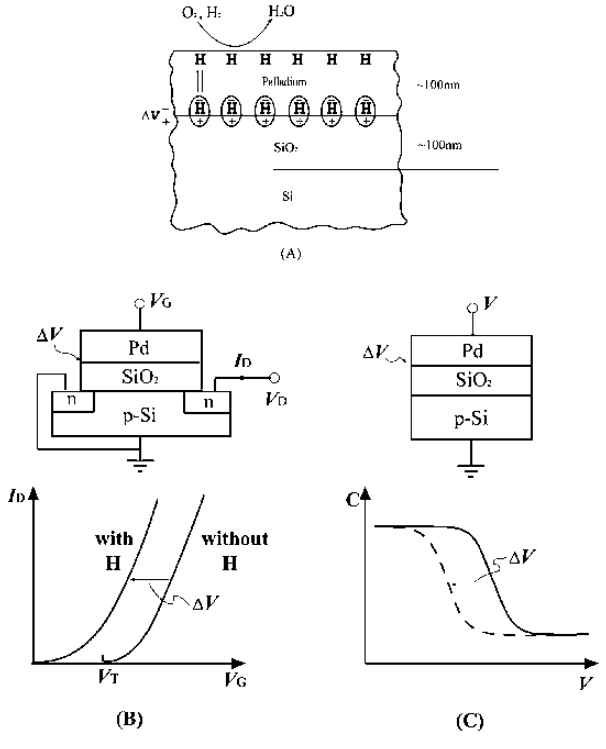

Figure 3 (A) Schematic picture of the metal-insulator region upon chemisorption of hydrogen atoms; (B) the hydrogen-induced shift of the threshold voltage characteristics of MISFET; (C) the hydrogen-induced shift of the capacitance-voltage curve in MOS capacitor (after ref. 23).

through the change in the flat band voltage of the semiconductor. In the presence of hydrogen in the ambient, hydrogen molecules are dissociated on the Pd surface into hydrogen atoms, which then diffuse through the Pd-layer and accumulate at the Pd-insulator interface as shown in Fig. 3A [23]. These hydrogen atoms give rise to a dipole layer creating a voltage drop, ΔV, which changes the work function of the metal at the interface. The voltage drop, ΔV can be measured from the electrical response (current or capacitance) of the Pd-MOS/MISFET device. For a field effect transistor, at a gate threshold voltage, V_T, sufficient minority carriers (electron for *p*-type Si) are accumulated at the semiconductor surface to yield a conducting channel. The threshold gate voltage, upon exposure to the hydrogen-containing atmosphere, shifts by ΔV, compared to the threshold voltage without any hydrogen induced voltage drop at the interface, V_T^O, which is then expressed as

$$V_T = V_T^O - \Delta V \tag{3}$$

where $\Delta V = \Delta V_{max}[\alpha\sqrt{P_{H_2}}/(1+\alpha\sqrt{P_{H_2}})]$ is experimentally observed with α and ΔV_{max} being constants (Fig. 3B).

Similarly, when the high frequency (1 MHz) small signal capacitance of a MOS device, determined by the extent of a depletion layer at the semiconductor surface, is measured with a bias voltage, it shifts along the voltage axis by ΔV as shown in Fig. 3C.

2.3. Surface conductive sensors

This type of sensor utilizes the change in the concentration of conduction electrons as a result of chemical reactions at the surface with adsorbed gas species. These reactions, chemisorption followed by a catalytic reaction, modify the defect states of the oxide surface layer to a depth of a few μm or less. Therefore, the operating temperature should be low enough to allow sufficient surface adsorption and to slow down the bulk defect equilibration processes, but high enough for catalysis reactions and charge transfer between the surface layer and the bulk interior. The working temperature of this type of sensor is usually lower than that of the bulk conduction based gas sensors, typically 200–500°C, depending on the base oxide and the target application.

In this chapter, we will mainly deal with this type of sensor from principles to the practical applications.

3. Gas-solid reactions and mechanism of surface conductive sensors

3.1. Physical and chemical adsorption

Atoms or molecules in the gas phase can be attracted and retained on the surface in two modes: (a) physisorption and (b) chemisorption. In the Lennard-Jones model, the energy of the system is represented as a function of adsorbate/adsorbent distance as shown in Fig. 4. The system can be defined as having zero energy when the adsorbate "molecule" resides at an infinite distance from the surface. As the molecule approaches the surface (curve a), it can polarize and induce an equivalent dipole in the substrate, which leads to a van der

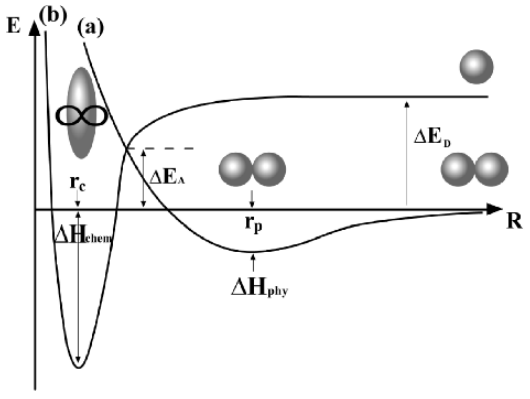

Figure 4 The energy of the system as a function of adsorbate/adsorbent distance (Lennard-Jones model for physical and chemical adsorption): (a) physical adsorption and (b) chemical adsorption.

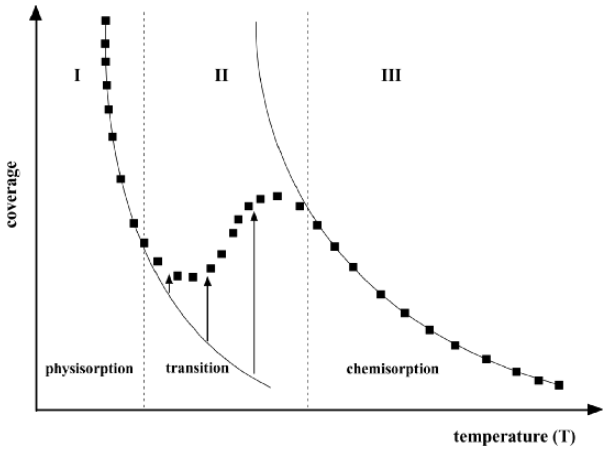

Figure 5 Typical adsorption isobar: (I) physisorption, (II) irreversible transition and (III) chemisorption.

Waals dipole/dipole interaction with a binding energy of ΔH_{PHY}, generally less than 0.2 eV (≈5 kcal/mol). But a further approach results in an atom-substrate repulsion to increase the energy of the system. Therefore, the physisorbed molecule is stably located at energy minimum (r_{p}) at a substantial distance from the surface. Because of the lack of activation energy for this process, the rate of physisorption becomes independent of temperature. However, the desorption of molecules requires an activation energy of ΔH_{PHY}. Hence the rate of physisorption can be written as

$$\mathrm{d}\Gamma_{\mathrm{PHY}}/\mathrm{d}t = k_{\mathrm{ads}} P(\Gamma^{\mathrm{O}} - \Gamma) - k_{\mathrm{des}}\Gamma \exp(-\Delta H_{\mathrm{PHY}}/RT) \quad (4)$$

where Γ^{O}, Γ, P and k are density of surface adsorption sites, density of sites covered by adsorbate, gas pressure and rate constants, respectively. Because the second term (desorption) increases with temperature, physisorption is mainly dominant at low temperature and negligible at high temperature. At steady state, Equation 4 yields the Langmuir isotherm:

$$\theta = P/[P + (k_{\mathrm{des}}/k_{\mathrm{ads}}) \exp(-\Delta H_{\mathrm{PHY}}/RT)] \quad (5)$$

If the pressure is very low, it reduces to a sort of Henry's law expression

$$\theta \cong (k_{\mathrm{ads}}/k_{\mathrm{des}}) \exp(\Delta H_{\mathrm{PHY}}/RT) P \quad (6)$$

where the fractional coverage, θ, becomes directly proportional to the gas pressure.

On the other hand, a molecule can dissociate into "atoms" upon provision of a large dissociation energy (ΔE_{D}). As an atom approaches the surface (curve b), a strong interaction generally involving electron transfer occurs to form a chemical bond with the surface at a distance of r_{c}. The adsorbate could be involved in a chemical bonding, or attracted to a Lewis acid site (unoccupied cation acceptor state) to donate electrons, or to a Lewis base site (occupied anion donor state) to capture electrons for an electrostatic bonding. In these cases, the heat of chemical adsorption (ΔH_{CHEM}) is generally larger than 1 eV (≈23 kcal/mole), sometimes approaching the heat of compound formation. However, the direct chemisorption of molecules seems less likely because the large energy (ΔE_{D}) is needed for the dissociation into atoms. In practice, adsorption occurs through physisorption followed by chemisorption for which the much smaller energy of ΔE_{A} is needed. The rate of chemisorption from the molecular gas phase can be expressed as

$$\mathrm{d}\Gamma_{\mathrm{CHEM}}/\mathrm{d}t = k_{\mathrm{ads}} P(\Gamma^{O} - \Gamma) \exp(-\Delta E_{\mathrm{A}}/RT) - k_{\mathrm{des}}\Gamma \exp[-(\Delta H_{\mathrm{CHEM}} + \Delta E_{\mathrm{A}})/RT] \quad (7)$$

At steady state, the equilibrium coverage becomes

$$\Theta = \Gamma/\Gamma^{\mathrm{O}} = k_{\mathrm{ads}}/k_{\mathrm{des}} \exp(\Delta H_{\mathrm{CHEM}}/RT) \quad (8)$$

Because both the adsorption and desorption processes require energies, they occur at an elevated temperature compared with physisorption.

Experimentally, the activation energy, ΔE_{A}, increases with increasing coverage at a given temperature, as can be qualitatively understood from Fig. 5. Because of the heterogeneity of the surface, the adsorbate starts filling from the site with lowest energy (highest ΔH_{CHEM}) and, hence, ΔH_{CHEM} decreases with increase in coverage. According to the Lennard-Jones model, the curve (b) will shift up as chemisorption proceeds, i.e., as ΔH_{CHEM} decreases, while curve (a) remains unaffected, which gives rise to an increase of ΔE_{A} with coverage.

The typical adsorption isobar (the coverage as a function of temperature for a constant gas pressure) is sketched as a dotted curve in Fig. 5. At low temperature (region I), adsorption follows an unactivated physisorption process of curve (a) corresponding to Equation 6 and at high temperature (region III), equilibrium chemisorption occurs according to curve (b) in Equation 8. In the intermediate temperature range, the transition from physisorption to chemisorption occurs such that equilibrium physisorption is readily reached, but chemisorption falls short of the equilibrium coverage (region II). The decline in chemisorption may result from the progressive increase of ΔE_{A} with coverage. When a clean surface is initially exposed to the adsorbing gas in this temperature regime, the

value of ΔE_A is so low that chemisorption proceeds very rapidly. However as the surface is covered, ΔE_A increases and the rate of adsorption decreases. Finally, adsorption occurs at a negligible rate. When the temperature is raised, thermal energy to overcome an activation barrier ΔE_A increases to provide more coverage with temperature. Hence, coverage increases with temperature in region II where the theoretical desorption rate (the second term in Equation 7) is substantially lower than the adsorption rate until the equilibrium coverage in region III is reached. Therefore, a simple evacuation (lowering the pressure) or lowering the temperature does not affect the amount of coverage. To "remove" the adsorbate, the temperature has to be raised in region III, where the desorption rate becomes appreciable. This is why "thermal cleaning" at high temperature is frequently performed to refresh the sensor. Thus, adsorption in the intermediate region is sometimes called "irreversible chemisorption" where the coverage depends on the history of material preparation. On the other hand, in region III, the desorption rate becomes balanced with the adsorption rate to reach an equilibrium coverage according to curve (b).

Experimentally, chemoresistive ceramics such as ZnO, TiO_2 and SnO_2 usually exhibit the so-called sigmoidal resistance behavior in humid air as shown in Fig. 6, similar to the behavior in Fig. 5. The low-temperature resistance minimum generally occurs at 200–250°C and the high-temperature maximum at 350–400°C, depending on the kind and the preparation method of the material. Although a complete understanding of these phenomena is lacking, it is closely related to the gas adsorption process. The surface conductivity is proportional to the total concentration of adsorbates, among which O^- and OH^- increase the resistance, but H_2O^+ donates an electron to decrease the resistance of the ceramics. Hence the resistance of a given sensor geometry can be expressed as [24]

$$R \propto [O^-]_s + [OH^-]_s - [H_2O^+]_s \qquad (9)$$

where $[\ ]_s$ is the concentration of adsorbates on the surface.

In the low temperature region I, adsorbed water molecules which act as donors block the equilibrium chemisorption of oxygen, giving lower $[O^-]_s$. Then the electrical resistance is governed by the amount of water adsorbed [25–29]. The electrons that are donated from water and those thermally excited from the valence band are accumulated near the surface to give an initial drop in resistance as shown in Fig. 6. As the temperature rises in region II, molecular water desorbs due to its weak bonding with the surface, permitting an equilibrium surface oxygen concentration. The dissociative chemisorption of water also occurs to generate a negatively charged hydroxyl group, resulting in a rise in the resistance:

$$H_2O + O_s^- + e^- = 2OH^- \qquad (10)$$

The decrease in resistance in region III results from the combination of both the desorption of OH^- and the NTC (negative temperature coefficient) property of the material.

3.2. Surface states

The surface state is a localized electronic energy level at the surface. In ionic crystals such as semiconducting metal oxides, surface states can be classified into two kinds depending on the source: (1) intrinsic surface states resulting solely from the distortion of lattice periodicity at the surface and (2) extrinsic surface states originated from the adsorption of gases or impurities on the surface. Tamm first calculated the intrinsic localized electronic energy state, the so-called Tamm state, by considering the asymmetry of the electronic periodic potential resulting from the sudden interruption in the periodicity of the crystalline lattice [30]. Tamm states, which arise particularly for an ionic crystal, appear whenever a substantial difference exists in the electron affinity between the surface species and the bulk species. Surface cations are expected to provide acceptor-like surface states (electron traps) near the conduction band while surface anions provide donor-like surface states (hole traps) near the valence band. This can be easily understood by the classic Madelung model for ionic crystal as schematically shown in Fig. 7 [31].

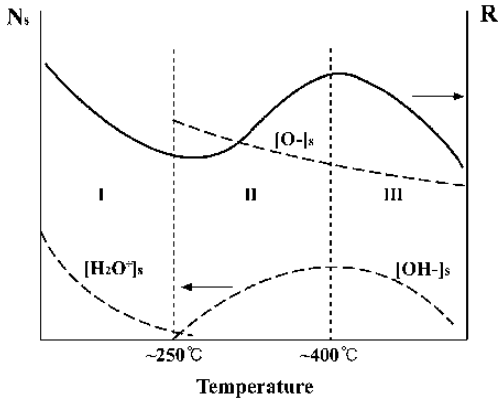

Figure 6 Schematic plots of equilibrium isobars for $[O^-]$, $[OH^-]$ and $[H_2O^+]$ and the resistance of SnO_2 as a function of temperature (after ref. 26).

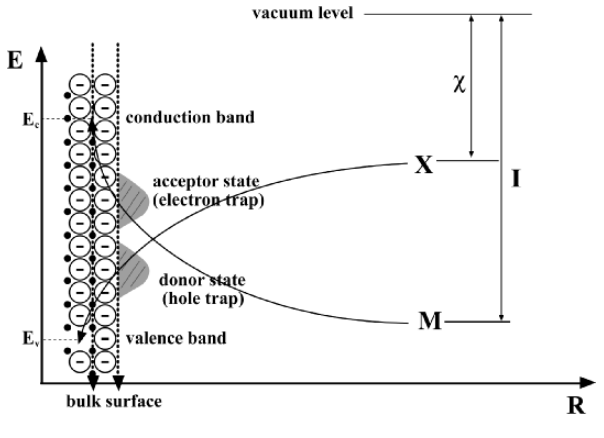

Figure 7 Madelung model for ionic solid MX [2] χ is the electron affinity and I is the ionization potential (after ref. 31).

According to the Madelung model, the electron affinity of the electronegative atom X at infinity ($R \rightarrow \infty$) becomes progressively larger when it is moved to its normal position in the ionic crystal MX due to the positive electrostatic potential of surrounding M^+ ions in the crystal. Similarly, the metal atom M has a high ionization potential, I (energy to remove the electron from a metal atom) at $R \rightarrow \infty$, which progressively decreases at its lattice position surrounded by the negative X^- ions. Within the crystal lattice, the empty energy level for the electron on an X atom becomes lower than that for a filled state on an M atom, which causes the electrons to leave M and form X ions. The unoccupied energy levels of the M^+ ions become the bulk conduction band and the occupied energy levels of the X^- ions form the bulk valence band. From this simple model, the electron energy levels at the surface sites differ from those in the bulk, which produces the intrinsic surface states. The unoccupied orbital on the cation acts as an acceptor-like surface state (Lewis acid site) and the occupied orbital on the anion as a donor-like state (Lewis base site). Shockley also defined an intrinsic surface state, the so-called Shockley state, for a covalent material where the atoms at the surface form dangling bonds.

Foreign atoms adsorbed on a new surface can capture electrons from or inject electrons into the bulk to form a localized electron energy state at the surface (extrinsic surface state), whose energy levels are those of the isolated, free species modified by the Madelung potential of the lattice. For instance, the adsorption of oxygen on an ionic crystal can occur in the molecular or atomic form. The electron energy of oxygen adsorbate becomes lower than that of the Fermi level (average electron energy in the crystal) in the ionic crystal, which causes a transfer of electrons from the bulk to the adsorbed oxygen by the following process:

$$O_2 + e^- = O_2^- \quad (11)$$

$$O + e^- = O^- \quad (12)$$

These charged particles are bonded to the surface via electrostatic forces, which is sometimes called "ionosorption," a form of chemisorption. Since the occupancy of the electrons in the surface states also has to obey the Fermi statistics, the relative concentrations of O_2^- and O^- to O_2 and O can be written as

$$[O_2^-]/[O_2] = \exp[-(E_{O_2^-} - E_F)/kT] \quad (13)$$

$$[O^-]/[O] = \exp[-(E_{O^-} - E_F)/kT] \quad (14)$$

where $E_{O_2^-}$ and E_{O^-} are the surface energy levels for oxygen molecules and atoms, respectively. In addition, oxygen molecules can dissociate into atoms on the surface of the oxide by the chemical reaction:

$$O_2 = 2O \quad (15)$$

From Equations 13–15, the relative concentrations of O_2^- to O^- can be expressed as [32]

$$[O_2^-]/[O^-] = [O_2]^{1/2} \exp\left[-\left(E_{O_2^-} - E_{O^-} - 1/2\Delta G^{O}_{(15)}\right)/kT\right] \quad (16)$$

where $\Delta G^{O}_{(15)}$ corresponds to the standard Gibbs energy change for reaction (15). Because of the large positive value of $\Delta G^{O}_{(15)}$, the concentration of O^- increases with increasing temperature, but decreases with increasing oxygen partial pressure. The presence of these species on SnO_2 has been detected by TPD, FTIR and EPR, where the O_2^- molecule dominates at temperatures below 150°C, and above this temperature atomic O^- species dominate as shown in Fig. 8. On the other hand, in the case of ZnO [33] and bismuth molybdate ($Bi_2Mo_3O_{12}$) [34], O_2^- exhibits stability up to higher temperatures of 175°C and 250°C, respectively.

In the presence of extrinsic or intrinsic surface states, electrons flow due to the difference in the energy levels of the surface state and the Fermi level (average energy of electrons) of the bulk. For instance, the adsorption of oxygen at the surface of d^0 and d^{10} transition metal oxides such as SnO_2 (110), ZnO($10\bar{1}0$) and TiO_2 (110) leads to a transfer of free electrons from the conduction band to the adsorbed oxygen (extrinsic surface state). The negligible concentration of band-gap states at their geometrically ideal surface makes them useful for conductance sensors [40–43]. The surface state whose level is lower than the Fermi level in the bulk will capture electrons from the conduction band to form a depletion layer beneath the surface for *n*-type

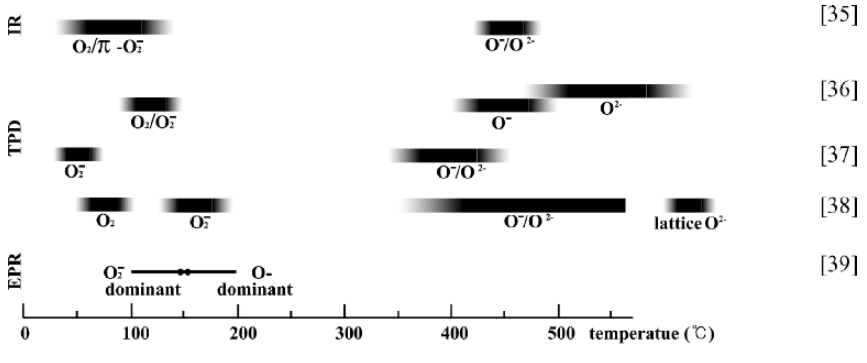

Figure 8 Adsorbed oxygen species detected on the surface of tin oxide at different temperatures with TPD (temperature programmed desorption), FTIR (Fourier transformed infrared) and EPR (electron paramagnetic resonance) analysis [after ref. 33].

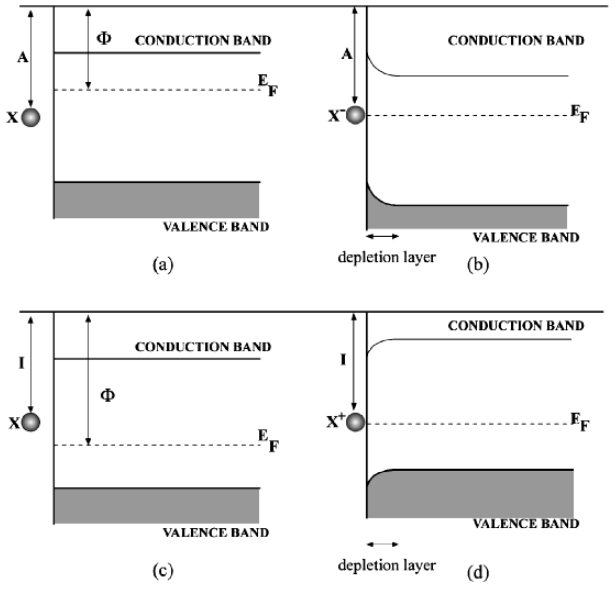

Figure 9 Depletive adsorption of X as X^- on an *n*-type semiconductor: (a) flat band (b) after adsorption, and adsorption of X as X^+ on a *p* type semiconductor: (c) flat band (d) after adsorption.

semiconductors and from the valence band to form a cumulative layer for *p*-type semiconductors. For example, the depletion layer is formed at the surface of SnO_2 (*n*-type) by the ionosorption of oxygen in the form of either O_2^- (<150°C) or O^- (>150°C). The accumulation layer is developed when the adsorbed oxygen captures electrons from the valence band of nickel oxide (*p*-type) to form O^-. The former is called "depletive adsorption" due to the limited source of electrons in the conduction band and the latter "cumulative adsorption" due to the abundant electrons existing in the valence band. For this reason, *p*-type oxides are found to be better catalysts than *n*-type oxides. Similarly, when the energy level of the surface state is higher than the Fermi level, electrons will be injected from the surface to the substrate, especially to the conduction band for *n*-type and to the valence band for *p*-type oxides to form an accumulation layer and a depletion layer, respectively. In Fig. 9, schematic pictures of depletive adsorption of X are drawn for *n*-type (Fig. 9b) and *p*-type semiconductors (Fig. 9d).

3.3. Boundary layer theory of adsorption

The theory of the space charge layer in a semiconductor was developed by Schottky [44, 45] and Mott [46]. Hauffe [47] extended this idea to the effect of adsorption on the characteristics of the space charge layer (depletion layer) of a semiconductor adsorbent. A quantitative derivation of the depletive space charge layer depicted in Fig. 10, upon transfer of electrons from the oxide to the surface states caused by the adsorption of gas species can be easily obtained from the one dimensional Poisson's equation for a semiconductor containing N_D^+ donor and N_A^- acceptor impurities per unit volume, both of which are completely ionized as +1 for donor and −1 for acceptor

$$d^2\Psi/dx^2 = -\rho(x)/\varepsilon_S \qquad (17)$$

where Ψ, ε_S and ρ are the potential, the permittivity of the semiconductor (i.e., the dielectric constant × vacuum permittivity) and the net charge density (C/m^3) consisting of electrons (n), holes (p), ionized donor (N_D^+) and ionized acceptor (N_A^-) in the material, respectively. According to the depletion approximation whereby the concentrations of mobile charges in the depletion region are assumed negligible, the net charge density within the space charge layer with a thickness of x_O can be written as

$$\rho = e(N_D^+ - N_A^-) \quad 0 \le x \le x_O \qquad (18)$$

where e is the amount of electron charge (1.602×10^{-19} coulomb) and the net charge density outside of the space charge layer ($x > x_O$) becomes zero. Substituting Equation 18 into Equation 17 and integrating twice, one obtains

$$\Psi(x) - \Psi_b = -\frac{e(N_D^+ - N_A^-)}{2\varepsilon_S}(x - x_0)^2 \qquad (19)$$

for the boundary conditions, $\Psi = \Psi_b$ at $x = x_O$ (bulk potential) and $d\Psi/dx = 0$ at $x = x_O$. The energy difference of unit negative charge, $V(x) \equiv \Psi_b - \Psi(x)$, is used instead of the potential, $\Psi(x)$ such that eV becomes the potential energy of an electron at x, compared with that in the bulk. Then the surface barrier height, V_S, defined as $V(0) - V(x_O)$ gives the Schottky relation:

$$eV_S = e^2(N_D^+ - N_A^-)x_O^2/2\varepsilon_S \qquad (20)$$

The activation energy, eV_S in Equation 20 has to be attained before the electron in the conduction band

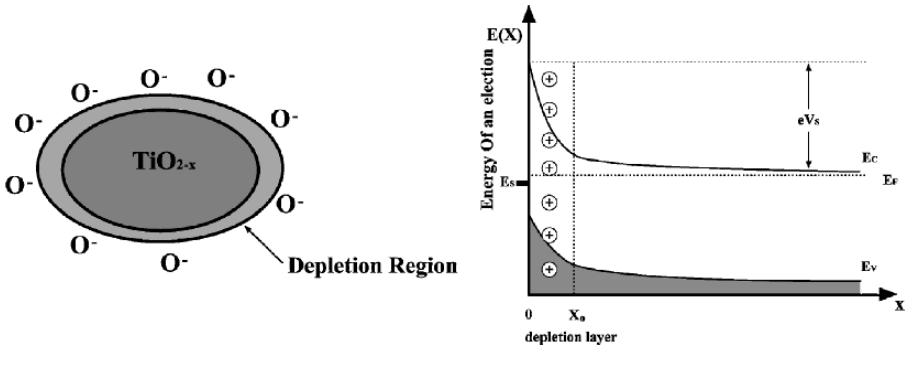

Figure 10 Space charge layer formed at the surface of an *n*-type semiconductor. E_S: surface state energy level.

moves to the surface state or atoms adsorbed on the surface.

Because of the conservation of charge, all the electrons or holes extracted from the space charge region of thickness x_O must be held by the surface states located at E_S. Hence the occupied surface state density (number of surface states per unit area), N_S becomes

$$N_S = \frac{1}{e}\int_0^{x_O} \rho(x)\mathrm{d}x = (\mathrm{N_D^+} - \mathrm{N_A^-})x_O \qquad (21)$$

Substituting Equation 21 into Equation 20, one can find a surface barrier height, which is proportional to the square of the occupied surface state density

$$\mathrm{eV_S} = e^2 N_S^2 / 2\varepsilon_S N_i \qquad (22)$$

where N_i corresponds to the net impurity concentration in the bulk ($= \mathrm{N_D^+} - \mathrm{N_A^-}$). For an *n*-type semiconductor for which $\mathrm{N_D^+} \gg \mathrm{N_A^-}$, the surface barrier height for electrons, $\mathrm{eV_S}$ is equal to $e^2 N_S^2/\varepsilon_S \mathrm{N_D^+}$. This is coincident with the experimental observations of increase in the activation energy for adsorption with coverage. The activation barrier height for further transport from the conduction band to the surface state, $\mathrm{eV_S}$ increases with increasing coverage (N_s) as noticed from Equation 22.

Weisz [48] first pointed out the maximum possible number of molecules ionosorbable by an electron transfer process, when a depletion layer is present, in terms of the fractional coverage. According to Equation 22, the number of adsorbate per unit area (m^2) of an *n*-type semiconductor surface becomes

$$N_S = (2\varepsilon_S \mathrm{N_D^+} V_S/e)^{1/2} \approx 1.1 \times 10^4 (\varepsilon \mathrm{N_D^+} V_S)^{1/2} \quad (23)$$

Where, ε is the dielectric constant of the oxide. Then the surface coverage becomes, for a total number of surface sites of the order of $10^{19}/\mathrm{m}^2$,

$$\theta \approx 1.1 \times 10^{-15} (\varepsilon \mathrm{N_D^+} V_S)^{1/2} \qquad (24a)$$

or

$$\theta \approx 0.3(\varepsilon B V_S)^{1/2} \qquad (24b)$$

where B is the concentration of donors ($\mathrm{N_D^+}/10^{29}$) in the oxide.

However, for a reasonable value of the dielectric constant of 10 and a fairly high surface barrier height of 1V, even the absurdly high assumption of $B = 1$(100% doping) does not allow complete surface coverage by chemisorption from Equation 24b. For a reasonable value of $B = 10^{-4}$ (impurity concentration of $\approx 10^{25}/\mathrm{m}^3$), one obtains a value of $\theta \approx 0.9\%$ only. As a result, more than 10^{-2}–10^{-3} monolayers of equilibrium ionosorption are practically not feasible no matter how much impurity is present in the oxide, because of the square root dependence of "impurity" concentration on N_S. A small amount of surface charge (about $(10^{16}$–$10^{17})e/\mathrm{m}^2$) is enough to raise the surface potential to block further electron transfer from the conduction band to the adsorbate. This is called the "Weisz limitation" for the ionosorption when a depletion layer is present.

In addition, the electron-occupancy of surface state at energy level E_S must obey the Fermi-Dirac statistics written as

$$f = 1/[1 + \exp(E_S - E_F)/kT] \qquad (25)$$

where f is the fractional occupancy of any nondegenerate level at an energy E_S and E_F corresponds to the Fermi energy of the substrate. As E_S approaches or crosses E_F by the amount of kT, there is a very abrupt change in the required fractional occupancy from 0 to 1 or vice versa. Hence, for an equilibrium concentration of occupied surface states, the Fermi energy of the oxide becomes virtually "pinned" at or near the energy of the surface state. The Fermi energy can be written from Equation 25 as

$$E_F = E_S + kT \ln \frac{f}{1-f} \qquad (26)$$

where $f/(1-f)$ is the ratio of the number of occupied states to the unoccupied states. With a maximum number of ionosorbable surface states of $10^{17}/\mathrm{m}^2$ according to Weisz limitation, the Fermi energy of the oxide is pinned at $(E_S - 0.2)$ eV at 500 K for a maximum possible number of total surface sites of $\approx 10^{19}/\mathrm{m}^2$. Therefore, surface state additives such as Pd and Ag are often used in a semiconductor or insulator to control the surface barrier height by pinning the Fermi energy at a certain level at the surface.

3.4. Electron theory of adsorption

Wolkenstein [49–55] extended the concept of boundary layer theory to adsorption in which occupation, as well as non-occupation of a surface state, occurs simultaneously. He distinguished two forms of chemisorption:

1. "Weak" chemisorption, in which the adsorbed particle C with its adsorption center remains electrically neutral, denoted as CL where L represents lattice.
2. "Strong chemisorption," in which the adsorbed particle captures a free electron or a free hole from the lattice such that the free electron or free hole participates directly in the bond. If free electron capture is involved, it is called a strong n-bond or acceptor bond denoted as "CeL." If free hole capture is involved, it is called a strong p-bond or donor bond denoted as "CpL."

By their nature, each of the strong bonds may be purely ionic, purely covalent or a mixed bond. Following Wolkenstein, the various forms of chemisorption of particle C on an ionic crystal composed of the singly charged ions, $\mathrm{M^+}$ and $\mathrm{R^-}$, are depicted in Fig. 11 where (a) and (d) correspond to "weak" bonding. An example of case (a) is a Na atom on $\mathrm{Na^+}$ in a NaCl crystal. This is essentially a one-electron bond, using the valence electron of the Na atom and none from $\mathrm{Na^+}$, like molecular ions $\mathrm{H_2^+}$ and $\mathrm{Na_2^+}$. In this case, the adsorbed

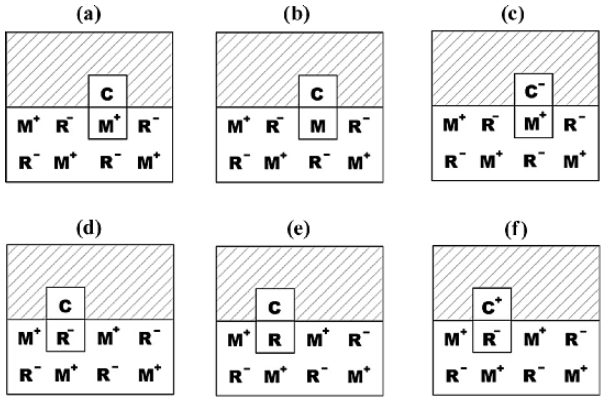

Figure 11 Types of chemisorption: (a) and (d) weak bond, (b) and (c) strong acceptor bond, (e) and (f) strong donor bond.

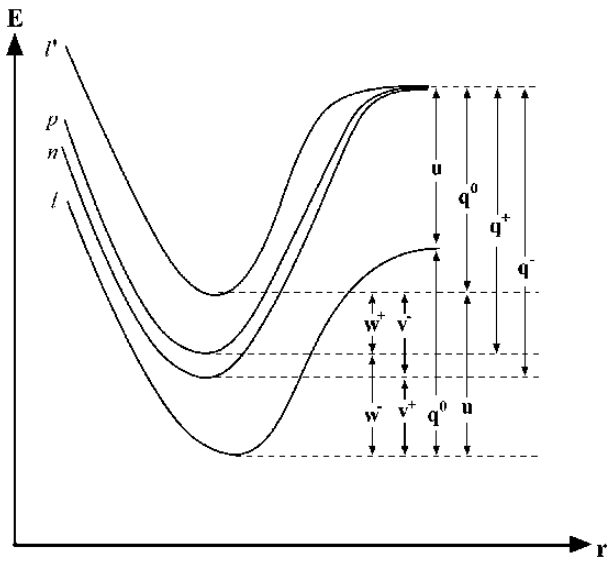

Figure 13 The energy of the system, E, as a function of the distance, r, between particle C and the substrate surface (adsorption curve).

Na atom together with Na^+ acquires a quantum mechanical dipole moment that may be several orders of magnitude greater than that induced in the physical adsorption. Case (d) is a similar weak bonding formed on an R^- ion center, for example, Cl atom on a Cl^- ion in a NaCl crystal.

"Strong" bonding is depicted in Fig. 11b, c, e and f. Two limiting cases exist: purely covalent (homopolar) and purely ionic (bipolar). The purely covalent bonding is shown in Fig. 11b and e, where C captures a free electron from the lattice to form a strong acceptor bonding by neutralizing M^+ in (b) and where C donates an electron to the lattice to form a strong donor bonding in (e). The adsorption of a Na atom on Na in a NaCl crystal can be an example of (b) and the adsorption of a Cl atom on a Cl is that of (e). They are comparable to the bond in Na_2 and Cl_2 molecules, respectively. Since an atom M or R, to which the particle C is attached, is rather weakly bound to the lattice compared with M^+ or R^- ions, the molecule CM or CR is expected to easily evaporate. The purely ionic bonding is shown in Fig. 11c and f, where C captures a free electron to form a strong acceptor bonding in (c) and where C donates an electron to form a strong donor bonding in (f). The former is the case of adsorption of Cl^- on a Na^+ center, and the latter the adsorption of Na^+ on Cl^- in a NaCl crystal. Both result in ionic bonding.

The various forms of strong and weak bonding are considered to be interconvertible because of thermal energy. The electron transition can be described in terms of the energy band scheme of a semiconductor shown in Fig. 12. A particle possessing affinity for a free electron is depicted by an acceptor level, A, and a particle possessing affinity for a hole by a donor level, D. The positions of levels A and D in the forbidden band gap depend on the nature of the lattice and the adsorbed particle, C. The electron transition reactions can be written down with the energy released or gained as follows:

Reaction ❶ represents the recombination of a free electron with a free hole. Reactions ❷ and ❸ correspond to the transition from "weak" to "strong" bonding accompanied by the disappearance of a free electron or hole from the lattice. They strengthen their bond via reduction of energy. On the other hand, reactions ❹ and ❺ correspond to the transition from "strong" to "weak" bonding by injecting an electron and a hole to the lattice. This process induces an excitation of the system.

The electron transition depicted in Fig. 12 can be incorporated into an adsorption energy diagram where the energy of the system, E, is plotted as a function of the distance, r, between particle C and the substrate surface as shown in Fig. 13. The curve l represents adsorption on a crystal that does not contain free electrons and holes whereas curve l' describes adsorption on an excited crystal containing a free electron and a

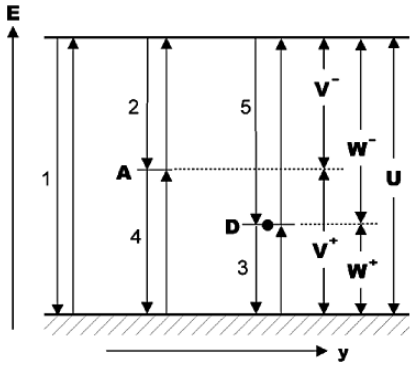

❶ $eL + pL \leftrightarrow L \quad \Delta E = u$

❷ $CL + eL \leftrightarrow CeL \quad \Delta E = v^-$

❸ $CL + pL \leftrightarrow CpL \quad \Delta E = w^+$

❹ $CeL + pL \leftrightarrow CL \quad \Delta E = v^+$

❺ $CpL + eL \leftrightarrow CL \quad \Delta E = w^-$

Figure 12 Band diagram scheme for electron transition of various types of chemisorption. A: acceptor level D: donor level.

free hole. Curves p and n correspond to the adsorption for strong donor and strong acceptor chemisorption, respectively. The minima of curves l, n, p and l' are the states CL, $CeL + pL$, $CpL + eL$, and $CL + eL + pL$, respectively. An inversion of the curves in Fig. 13 would correspond to the desorption process. The desorption processes for the states l, n, p and l' can be written as follows:

$$l)\ CL \rightarrow C + L \qquad \Delta E = q^{O} \tag{27}$$

$$n)\ CeL + pL \rightarrow C + eL + pL \qquad \Delta E = q^{-} \tag{28}$$

$$p)\ CpL + eL \rightarrow C + eL + pL \qquad \Delta E = q^{+} \tag{29}$$

$$l')\ CL + eL + pL \rightarrow C + eL + pL \qquad \Delta E = q^{O} \tag{30}$$

where, the following relations hold.

$$q^{+} = q^{O} + w^{+} \tag{31}$$

$$q^{-} = q^{O} + v^{-} \tag{32}$$

In the boundary layer theory, the removal of an electron from an acceptor level, A, or the injection of an electron to a donor level, D, is considered as a desorption of the adsorbate. However, in this treatment, this action does not represent the desorption of particles, but merely their transition from a state of "strong" to "weak" bonding with the surface. Hence, chemisorbed particles (especially electrically neutral adsorbates) can be described in terms of an energy level.

Consider a total number N_S of particles of a given kind chemisorbed on a unit surface, of which N^O particles are in a state of weak bonding (neutral form), N^- in a state of strong acceptor bonding and N^+ in a state of strong donor bonding. The equilibrium fractions of the different forms of chemisorption are expressed as

$$\eta^{O} = N^{O}/N_S, \quad \eta^{-} = N^{-}/N_S, \quad \eta^{+} = N^{+}/N_S \tag{33}$$

so that

$$\eta^{O} + \eta^{+} + \eta^{-} = 1 \tag{34}$$

At equilibrium on the surface, the probability of occupancy of an electron at acceptor level A or donor level D is given by the Fermi statistics

$$f = 1/[1 + \exp\{(E - E_F)/kT\}] \tag{35}$$

The probability that an acceptor level is occupied is the ratio of the number of occupied acceptor levels (N^-) to the total number of acceptor levels, occupied and unoccupied. The total number of acceptor levels is the total number of levels N_S less the occupied donor levels (N^+), that is, $N^O + N^-$. Therefore one obtains

$$N^{-}/(N^{O} + N^{-}) = 1/[1 + \exp\{(\varepsilon_S^{-} - v^{-})/kT\}] \tag{36}$$

$$N^{+}/(N^{O} + N^{+}) = 1/[1 + \exp\{(\varepsilon_S^{+} - w^{+})/kT\}] \tag{37}$$

where ε_S^- and ε_S^+ are the differences between the Fermi level and the conduction band and valence band, respectively.

From Equations 33–37, the equilibrium fractions of the different forms of chemisorption can be obtained as

$$\eta^{O} = 1/[1 + 2\exp(-\Delta u/kT)\cosh\{(\varepsilon_S^{+} - u^{+})/kT\}] \tag{38}$$

$$\eta^{-} = [\exp\{-(\Delta u/kT) + (\varepsilon_S^{+} - u^{+})/kT\}]/ [1 + 2\exp(-\Delta u/kT)\cosh\{(\varepsilon_S^{+} - u^{+})/kT\}] \tag{39}$$

$$\eta^{+} = [\exp\{-(\Delta u/kT) - (\varepsilon_S^{+} - u^{+})/kT\}]/ [1 + 2\exp(-\Delta u/kT)\cosh\{(\varepsilon_S^{+} - u^{+})/kT\}] \tag{40}$$

The dependence of η^O, η^+ and η^- on ε_S^+ is schematically shown in Fig. 14. As the Fermi level moves upward to become an n-type semiconductor, η^- increases monotonically, while η^+ decreases as depicted in Fig. 14b. On the other hand, η^O (the fraction of adsorbate with neutral weak bonding) passes through a maximum at $\varepsilon_S^+ = u^+$. As a result, when the Fermi level lies close to the top of the valence band, $\eta^+ \gg \eta^-$ holds such that practically all the chemisorbed particles become donors. Similarly if the Fermi level lies close to the conduction band, then $\eta^- \gg \eta^+$ holds such that all the adsorbates act as acceptors. In addition, the total

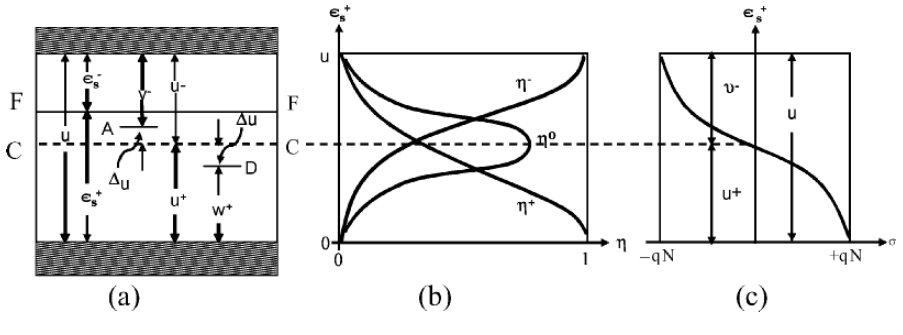

Figure 14 (a) Band diagram; (b) the dependence of the concentrations of various adsorbates on the Fermi level and (c) the amount of surface charge with the Fermi level. F: Fermi level; C: center of band gap.

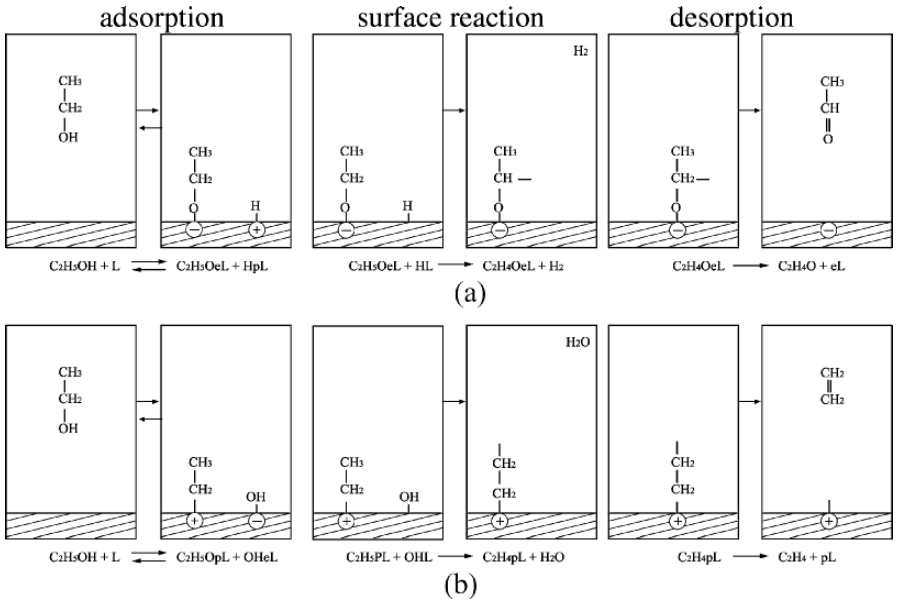

Figure 15 Schematics of a series of alcohol dissociation reactions (a) dehydrogenation and (b) dehydration reaction.

amount of surface charge varies with the location of Fermi level as shown in Fig. 14c, where as the substrate changes from n-type to p-type, the net charge of the adsorbate changes from negative to positive.

For the equilibrium between the surface and the gas phase, the adsorption isotherm has the form

$$aP = \mathrm{N}^{\mathrm{O}} e^{-q^{\mathrm{O}}/kT} + \mathrm{N}^{-} e^{-q^{-}/kT} + \mathrm{N}^{+} e^{-q^{+}/kT} \quad (41)$$

which, using Equations 38–40, can be simplified as

$$aP = \left(1 + e^{-\varepsilon_{\mathrm{S}}^{-}/kT} + e^{-\varepsilon_{\mathrm{S}}^{+/}/kT}\right)\eta^{\mathrm{O}} N e^{-q^{\mathrm{O}}/kT} \quad (42)$$

3.5. Dissociation of ethyl alcohol

It is well known that ethyl alcohol dissociates along two paths depending on which bond is broken in the stage of dissociative adsorption [56]: the O–H bond or the C–OH bond. The former corresponds to

$$\mathrm{C_2H_5OH} \rightarrow \mathrm{CH_3CHO} + \mathrm{H_2}\ \text{(dehydrogenation)} \quad (43)$$

and the latter

$$\mathrm{C_2H_5OH} \rightarrow \mathrm{C_2H_4} + \mathrm{H_2O}\ \text{(dehydration)} \quad (44)$$

Both reactions occur in three stages as schematically shown in Fig. 15: (i) adsorption of an alcohol molecule, (ii) surface reaction and (iii) desorption of the reaction products. For example, the dehydrogenation reaction (43) follows the procedure shown in Fig. 15a to produce acetaldehyde ($\mathrm{C_2H_4O}$).

$$\mathrm{C_2H_5OH_{(g)}} \leftrightarrow \mathrm{C_2H_5OeL_{(ads)}} + \mathrm{HpL_{(ads)}}\ \text{(adsorption)} \quad (45)$$

$$\mathrm{C_2H_5OeL_{(ads)}} + \mathrm{HL_{(ads)}} \rightarrow \mathrm{C_2H_4OeL_{(ads)}} + \mathrm{H_{2(g)}}\ \text{(surface reaction)} \quad (46)$$

$$\mathrm{C_2H_4OeL_{(ads)}} \rightarrow \mathrm{C_2H_4O_{(g)}} + \mathrm{eL}\ \text{(desorption)} \quad (47)$$

Denoting $A = \mathrm{C_2H_4O}$ and $R = \mathrm{C_2H_5O}$, the rates of production of radicals, R and A are

$$\mathrm{d}N_{\mathrm{R}}/\mathrm{d}t = \alpha P - (\beta_1 N_{\mathrm{R}} \bullet N_{\mathrm{H}^+}) - \gamma_1 (N_{\mathrm{R}} \bullet N_{\mathrm{H}^{\mathrm{O}}}) \quad (48)$$

$$\mathrm{d}N_{\mathrm{A}}/\mathrm{d}t = \gamma_1 (N_{\mathrm{R}} \bullet N_{\mathrm{H}^{o}}) - \delta_1 N_{\mathrm{A}} \quad (49)$$

According to quasi-steady state assumption, Equations 48 and 49 become zero to give

$$\alpha P = \beta_1 (N_{\mathrm{R}} \bullet N_{\mathrm{H}^+}) + \gamma_1 (N_{\mathrm{R}} \bullet N_{\mathrm{H}^{\mathrm{O}}}) \quad (50)$$

and

$$\gamma_1 (N_{\mathrm{R}} \bullet N_{\mathrm{H}^{\mathrm{O}}}) = \delta_1 N_{\mathrm{A}} \quad (51)$$

where P, N_{R}, N_{H} and N_{A} are the vapor pressure of the alcohol and the surface concentrations of the corresponding molecules, respectively. Equation 51 leads to the rate of production of acetaldehyde, g_{A} which, depending on the relative amount of $\mathrm{HpL_{(ads)}}$ ($\mathrm{H^+}$) and $\mathrm{HL_{(ads)}}$ ($\mathrm{H^O}$), can be

$$g_{\mathrm{A}} = \alpha P - \beta_1 N_{\mathrm{R}} \bullet N_{\mathrm{H}^+} \cong \alpha \frac{\gamma_1}{\beta_1} \frac{\theta_{\mathrm{H}^{\mathrm{O}}}}{\theta_{\mathrm{H}^+}} P \quad (52)$$

if $\beta_1 (N_{\mathrm{R}} \bullet N_{\mathrm{H}^+}) \gg \gamma_1 (N_{\mathrm{R}} \bullet N_{\mathrm{H}^{\mathrm{O}}})$, i.e., $\theta_{\mathrm{H}^{\mathrm{O}}}/\theta_{\mathrm{H}^+} \ll \beta_1/\gamma_1$ or

$$g_{\mathrm{A}} = \alpha P \quad (53)$$

if $\beta_1 (N_{\mathrm{R}} \bullet N_{\mathrm{H}^+}) \ll \gamma_1 (N_{\mathrm{R}} \bullet N_{\mathrm{H}^{\mathrm{O}}})$, i.e., $\theta_{\mathrm{H}^{\mathrm{O}}}/\theta_{\mathrm{H}^+} \gg \beta_1/\gamma_1$.

Similarly, the dehydration reaction occurs by the following process according to Fig. 15b

$$\mathrm{C_2H_5OH + L} \leftrightarrow \mathrm{C_2H_5pL + OHeL}\ \text{(adsorption)} \quad (54)$$

$$\mathrm{C_2H_5pL + OHL} \rightarrow \mathrm{C_2H_4pL + H_2O}\ \text{(surface reaction)} \quad (55)$$

$$\mathrm{C_2H_4pL} \rightarrow \mathrm{C_2H_4 + pL}\ \text{(desorption)} \quad (56)$$

to give the production rate of adsorbate radicals

$$dN_Q/dt = \alpha P - \beta_2 N_{Q^+} \bullet N_{OH^-} - \gamma_2 N_{Q^+} \bullet N_{OH^o} \quad (57)$$

$$dN_E/dt = \gamma_2 N_{Q^+} \bullet N_{OH^o} - \delta_2 N_{E^o} \quad (58)$$

where $E = C_2H_4$ and $Q^+ = C_2H_5pL$. At steady state, Equations 57 and 58 become zero to give

$$\alpha P = \beta_2 N_{Q^+} \bullet N_{OH^-} + \gamma_2 N_{Q^+} \bullet N_{OH^o} \quad (59)$$

$$\gamma_2 N_{Q^+} \bullet N_{OH^o} = \delta_2 N_{E^o} = g_E \quad (60)$$

Hence, the reaction rate for ethylene, g_E becomes

$$g_E = \alpha \frac{\gamma_2}{\beta_2} \frac{\theta_{OH^o}}{\theta_{OH^-}} P \quad (61)$$

When $\beta_2 N_{Q^+} \bullet N_{OH^-} \gg \gamma_2 N_{Q^+} \bullet N_{OH^o}$, i.e., $\theta_{OH^o}/\theta_{OH^-} \ll \beta_2/\gamma_2$ or

$$g_E = \alpha P \quad (62)$$

When $\beta_2 N_{Q^+} \bullet N_{OH^-} \ll \gamma_2 N_{Q^+} \bullet N_{OH^o}$, i.e., $\theta_{OH^o}/\theta_{OH^-} \gg \beta_2/\gamma_2$.

As a result, the dehydrogenation rates, g_A in Equation 52 and the dehydration rates, g_E in Equation 61 depend on the position of the Fermi level of the substrate because of the relations:

$$\theta_{H^o}/\theta_{H^+} = \exp\left(\frac{\varepsilon_S^+ - w_{H^+}}{kT}\right),$$

$$\theta_{OH^o}/\theta_{OH^-} = \exp\left(\frac{\varepsilon_S^- - \nu_{OH^-}}{kT}\right) \quad (63)$$

as given by Equations 38–40 before they are saturated to αP. The lowering of the Fermi level retards dehydrogenation and accelerates the dehydration reaction as depicted in Fig. 16. The selectivity of the catalyst can be achieved by doping donor impurities for the dehydrogenation reaction and by doping acceptor impurities for the dehydration reaction [57]. The reaction that is accelerated by the electron is called an *n*-type reaction, and on the contrary, the reaction that is favored for lowering the Fermi level is called a *p*-type reaction.

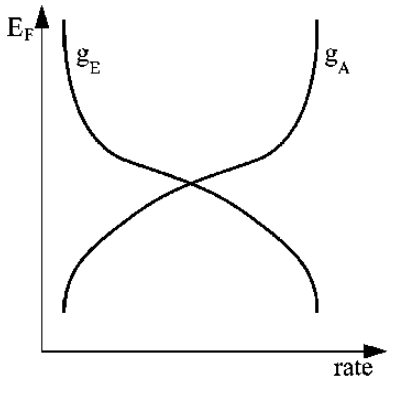

Figure 16 The rates of dehydrogenation reaction (g_A) and dehydration reaction (g_E) as a function of the Fermi energy level.

3.6. Sensing mechanism

Chemoresistive oxide sensors often change their resistances more than a factor 100 upon exposure to a trace of reducing gases such as H_2, CH_4, ethanol, CO and propane. Oxygen adsorbed on the surface of the sensor extracts an electron from the bulk to ionize into O^- or O_2^- (O^- is believed to be dominant at the operating temperature of 300–450°C), which increases the resistance. Upon exposure to a reducing gas such as CO, the CO reacts with the adsorbed O^-, releasing the trapped electron to the conduction band and subsequently lowering the resistance. The amount of resistance change is proportional to the concentration of the reducing gas in the ambient, which is believed to be the dominant sensing mechanism of the surface conductive gas sensor. However, as Weisz pointed out [48], the concentration of charged oxygen molecules or atoms are limited to <1% of the total number of surface states. It is impossible that a change in <1% of surface coverage causes a factor 100 change in the total resistance. Therefore, the surface barrier at the intergranular contact must play an important role in achieving high sensitivity of the sensor.

The intergranular contact consisting of the space charge layer depleted of electrons is usually more resistive than the bulk. The total conductance of a porous medium is then determined by the percolation path through the structural inhomogeneities with the low resistance of bulk grain in series with the high resistance of intergranular contacts. Electrons must overcome the intergranular contact barrier in order to cross from one grain to another for conduction. In this case, the sensor resistance can be written as

$$G = G_0 \exp(-eV_S/kT) \quad (64)$$

The barrier height is proportional to the square of the coverage as shown in Equation 22 and subsequently the conductivity has an exponential dependence to the square of the coverage.

In general, the intergranular contacts can be classified into three cases, which give different dependences for conductance on the partial pressures of oxygen and combustible gases [58–60]:

1. Bulk-trap-limited conduction process (Open Neck)
2. Surface-trap-limited conduction process (Closed Neck)
3. Schottky barrier-limited conduction process (Schottky Contact)

These processes can be distinguished by comparing the width of the neck at the intergranular contact versus the Debye length of electron, L_D

$$L_D = \sqrt{\varepsilon_S kT/(e^2 n_b)} \quad (65)$$

where ε_s, e and n_b are the permittivity of the oxide, the elementary electron charge and the bulk electron density, respectively. If the neck width $\gg L_D$, the conductivity depends on the width of the undepleted layer

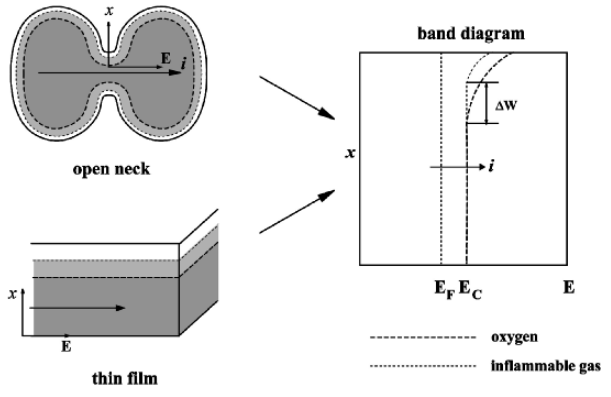

Figure 17 Conduction process in a well-sintered ceramic and thin film gas sensor.

and the rate of activation of electrons from the Fermi level in the bulk to the conduction band edge (bulk-trap-limited conduction) expressed as

$$G \propto w \exp[-(E_c - E_F)_b/kT] \tag{66}$$

where w, E_c and E_F correspond to the undepleted layer width, the conduction band edge and the Fermi level of the bulk oxide. In this case, sensitivity to the gas concentration can only be achieved by the modulation of the effective width of the surface space charge layer, w in Equation 66. This behavior can be found in a well-sintered ceramic pellet with "open necks" or in compact and thin film structure with thickness much larger than L_D, as shown in Fig. 17.

On the other hand, when the conduction width is smaller than $2L_D$, the space charge layers from the opposite surfaces overlap to form a higher-resistance ohmic path through the depleted zone as shown in Fig. 18. This is often found in a less sintered ceramic with "closed necks" and in thin films and pressed ceramics with nano-crystallites. In this case, flat-band conditions are fulfilled to a good approximation and the conductance is determined by the activation of electrons from the surface states to the conduction band edge at the surface (surface-trap-limited conduction)

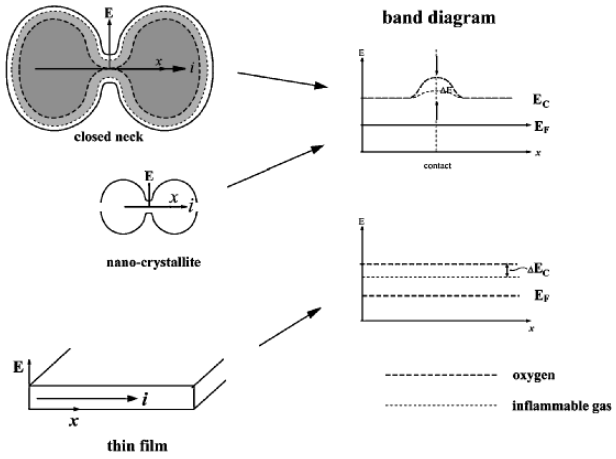

Figure 18 Schematic band structure for a less sintered ceramic, nano-crystallite and very thin film gas sensor with and without inflammable gas.

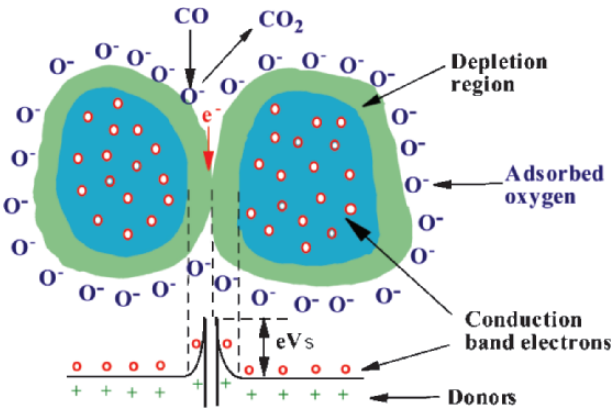

Figure 19 Compressed powder model illustrating CO sensing mechanism in an *n*-type oxide.

expressed as

$$G \propto \exp[-(E_c - E_s)_S/kT] \tag{67}$$

where $(E_c - E_s)_S$ corresponds to the difference between the conduction band edge at the surface and the surface state energy level. The sensitivity is achieved by the modulation of the surface conduction band energy, resulting from the direct change in the occupancy of surface states [61].

When ceramic particles with diameter larger than $2L_D$ are "pressed" together as shown in Fig. 19, Schottky barrier-limited conduction with the surface barrier height, as appears in Equation 22 is expected. The conductance is limited by the electron transport across the barrier at the intergranular contact, which can be written as [62, 63]

$$G \propto \exp[-eV_S/kT] \tag{68}$$

Here, eV_S is the surface barrier height, which is directly proportional to the square of the occupancy of the surface states as in Equation 22. Hence resistance-response of the sample becomes a sensitive function of the concentration of the inflammable gas in the ambient as mentioned earlier.

A good example of the resistance behavior arising from the Schottky contact can be found in work of Shierbaum *et al*. [64]. They reported changes in the work function, $\Delta\Phi$ and $\Delta\Phi_O$ for a SnO_2 gas sensor, when the gas composition in the surroundings is varied from the ambient condition to a CO concentration of interest, and to the standard composition, respectively. They presented the relationship, $\Delta\Phi/\Delta\Phi_O = \log(P_{CO}/P_{CO}^O)^n$ between the work function change and the CO concentration in the humid air, i.e., $\Phi \propto \log P_{CO}^n$ for constant values of $\Delta\Phi_O$ and P_{CO}^O as shown in Fig. 20a. Since the work function, Φ (the difference between the Fermi level and the vacuum level) can be written as

$$\Phi = -eV_S + \chi + \xi \tag{69}$$

where eV_S, χ and ξ are the surface band bending energy, electron affinity at flat band condition and the

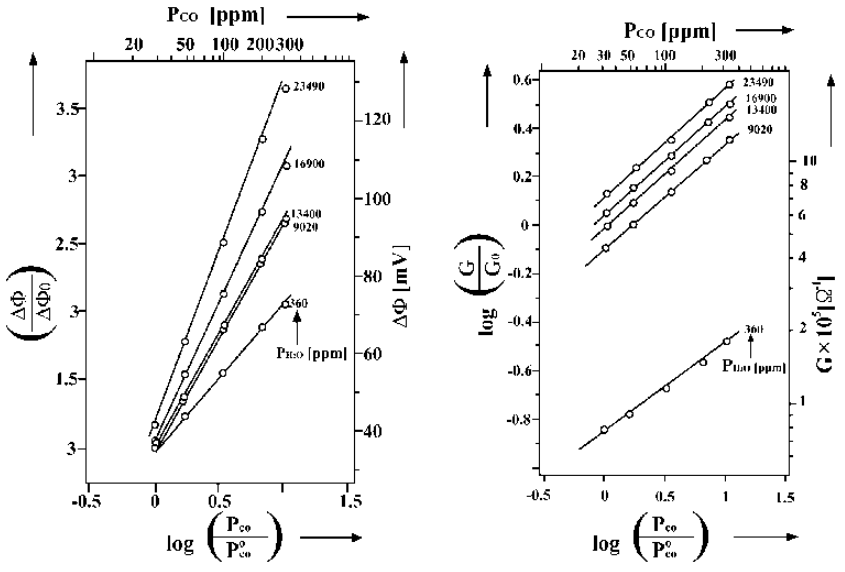

Figure 20 (a) Relative work function change and (b) relative conductance change with CO concentration, compared with standard composition of gas (30 ppm CO and 13,860 ppm H_2O) [after ref. 64].

difference between the Fermi level and the bottom of the conduction band, respectively, a linear relationship between $\log(G/G_O)$ and $\Delta\Phi/\Delta\Phi_O$ is expected from Equation 64 which is confirmed from Fig. 20. Hence, the conductance is determined by the variation in the barrier height at the intergranular contact. An increase in CO concentration gives rise to a decrease in eV_S and subsequently increases the conductance and vice versa.

However, a sintered ceramic is likely to incorporate more than one type of intergranular contact. Each crystallite is connected to several neighbors by either neck-type or barrier-type contacts. Since the barrier-type contacts usually show much larger resistance than the neck-type contacts, it is more favorable for electrons to pass through the necks rather than through the barrier contacts. According to percolation theory, if the neck concentration becomes higher than the percolation threshold (e.g., $1/(z-1)$ for Bethe lattice; z is the coordination number), a low resistance percolation path exists where all the contacts consist of a series of necks. Below the threshold, isolated islands of neck-contacts in a matrix of barrier-type contacts exist. In other words, the diameter of an island consisting of neck-contacts is less than the dimension of the sensor such that a conducting channel made of a series of neck-contacts cannot be found. In this case, electrons can either encounter only barrier type contacts or, more likely, a percolation through the mixture of barriers and necks, depending on the size and shape of the neck-islands.

Practical sensor elements are usually sintered at an elevated temperature to obtain sufficient mechanical strength, but as sintering proceeds, the nature of the contacts changes from barrier type to necks in a short period of time. Therefore, the response characteristics of a real sensor are critically dependent on the fabrication method and thermal treatment of the ceramic. Various empirical laws have been proposed to explain the response of the SnO_2-based gas sensor as listed in Table II.

4. Fabrication and design considerations of gas sensors

4.1. Sensor structures and materials

Metal oxide sensors can be made as pellets, thick films or thin films, and composed of large-grained or nanocrystalline materials, utilizing various technologies: (1) a conventional sintering process for bulk-pellet type (2) a screen printing technique for thick film type and (3) a vacuum deposition process for thin film type. Some of these materials are promising because their fabrication can be done reproducibly, others because of their low cost, and some due to their faster response to gases. Table III lists a number of different sensor preparation methods that have been investigated for CO gas sensing [70].

4.1.1. Bulk type

Many commercially available devices produced by a conventional ceramic sintering process have either rectangular substrates (TGS 109) or cylindrical tubular

TABLE II Empirical formulae describing the dependence of the conductance of a SnO_2-based gas sensor on specific gas species

Formula	Gas species	Comments	References
$G = Ap_R^{\beta}$	Combustible gas	$0.5 < \beta < 1$	[65–67]
$G = Bp_{O_2}^{-\beta}$	O_2	$0.25 < \beta < 0.55$	[68]
$G = G_O P_{O_2}^{-\beta}(1 + K_{H_2O}P_{H_2O} + K_{CO}P_{H_2O}P_{CO})^{\beta}$	H_2O,CO	$\beta \approx 0.42$	[68]
$G = G_O + A_O P_R^{\beta}$	Reducing gas	$\beta \approx 0.5$	[69]

TABLE III CO sensors made of thick/thin films and/or nano-crystalline materials [70]

Material	Film type	Film thickness	Grain size	Temp range (°C)	Opt. temp	CO sens.[a]	Other gases	Detect. limit (ppm)	Resp. time
SnO_2	Thin	400–500 nm	60–100 nm	175–375	275	0.68 (150)	–	25	2 min
SnO_2	Thin	N.A.	11–30 nm	50–500	>400	0.10 (300)	EtOH	300	N.A.
SnO_2	Thick	10–20 um	100 nm	200–450	400	0.87 (1000)	CH_4	1000	N.A.
SnO_2	Thin	150 nm	5–7 nm	200–350	300	0.7 (50)	CH_4	50	N.A.
SnO_2	Thin	100 nm	10.6 nm	150–300	270	0.24 (150)	–	40	50 s
TiO_2	Thick	62 um	500 nm	600	600	1.2 (250)	–	250	N.A.
TiO_2	Thin	85 nm	10 nm	150–300	200	0.0333	CO, CH_4	100	N.A
TiO_2	Thin	N.A.	34 nm	50–210	190	10 (100)	NO_2	100	1–3 min
TiO_2	Thick	10 microns	28 nm	400–500	450	0.45 (100)	NO_2	100	N.A.

[a]Data are reported as R_G/R_B where R_G is the resistance with CO and R_B is the resistance in the background gas. Numbers in parenthesis are the gas concentrations in ppm of the reported sensitivity.

substrates (TGS813), as shown in Fig. 21. They are integrated with a direct or an indirect heating coil (Ir-Pd or Cr alloy wire), which ensures operating temperatures of 300–450°C. In spite of their complicated structures and large power consumption (>500 mW), these ceramic sensors have good long-term stability and, hence, are widely used for toxic and inflammable gas leak detectors.

4.1.2. Thick film type

The size of the sensor can shrink down to about 1 × 1 mm and subsequently can achieve low power consumption of less than 200 mW in thick film sensors made by the screen-printing method as shown in Fig. 22. The screen-printing paste is prepared by mixing chemically sensitive powder, for instance SnO_2 with organic deflocculant additives such as propadyol or terpineol, and inorganic binders such as ethyl silicate and noble metal catalyst. They are printed onto an Au- or Pt electrode-printed alumina substrate with heater on the backside.

4.1.3. Thin film type

These sensors are presently not so widely used as the thick film and the bulk structures. However, because of their device integration capability and possibility of higher unit-to-unit consistency of performance, these sensors are expected to gain interest in the future. Low-power devices below 150 mW can be made in the thin film structure on a conventional silicon wafer, alumina substrate, or even sapphire substrate utilizing deposition methods such as evaporation [72, 73], sputtering [74], and spin-coating of sol-gel material [75].

4.1.4. Grain size control

Fine and homogeneous nano-ceramic powders can be prepared by the wet precipitation method. For instance, SnO_2 with diameter <10 nm can be prepared by the hydrolysis of $SnCl_4$ with ammonia solution, followed by washing, drying and calcination to remove the Cl residue from the particles. Yamazoe *et al*. [76, 77] studied the effects of grain size, when it becomes comparable to the Debye length of electrons, L_D, on the

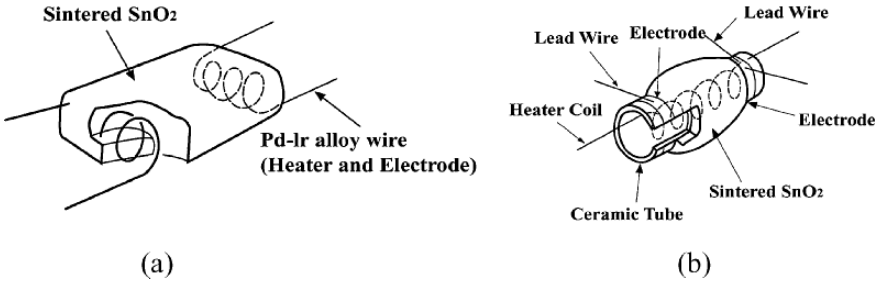

Figure 21 Bulk type gas sensors with: (a) direct heating (b) indirect heating (after ref. 69).

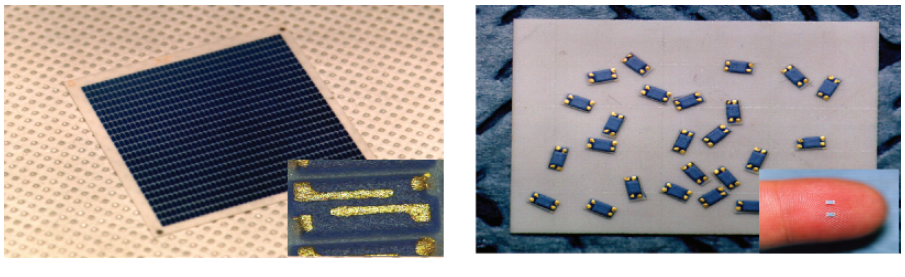

Figure 22 Thick film gas sensors (1 × 2 mm) [taken from CAOS Inc.].

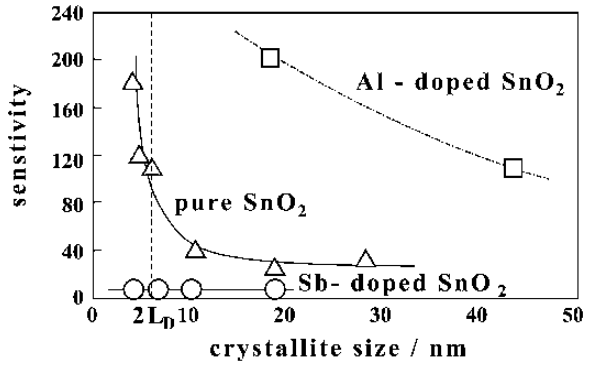

Figure 23 Sensitivity of doped and undoped SnO_2 sensor to 8000 ppm H_2 gas versus particle size [after ref. 70].

sensitivity of the sensors. They controlled and stabilized nano-crystallites in the range of 5–30 nm by dispersing appropriate grain growth inhibitors such as CaO, NiO and ZnO with SnO_2. The sensitivity increased (Fig. 23) as the grain size decreased, with an especially drastic increase when the diameter of the crystallite was $\sim 2L_D$ ($\approx$6 nm), where total depletion of grains occurs.

Similarly, for a given crystallite size, the sensitivity can be also controlled by varying the concentration of doping impurities (Fig. 23) in the sensing element, thereby the Debye length of electrons according to Equation 65. If trivalent ions such as Al^{+3} are doped into the SnO_2 lattice to decrease the concentration of electron, n_b, the Debye length would increase, while the doping of pentavalent ions such as Sb^{+5} would decrease the Debye length.

4.1.5. Supported catalyst

To promote the sensitivity, the response time and sometimes the selectivity toward certain gases, a small amount of noble metal and ceramic catalysts are added to the sensor material in the form of fine dispersions with diameters of few nanometers. As the noble metal catalyst, one uses Pd, Ag, Rh, Ir and Pt, and as ceramic catalysts: V_2O_5, Re_2O_7, CuO and NiO. These catalysts are effective because of their large active surface area per gram of material as well as high concentrations of surface defects.

A good dispersion of the catalyst on the semiconducting support is essential to the performance of surface conductive type gas sensors. The noble metal catalysts, for example, can be incorporated into a SnO_2 support by:

(1) impregnating the starting SnO_2 powder with noble metal chloride such as $PtCl_4$ and $PdCl_2$ solution, followed by drying and calcination (impregnation method) [78];
(2) mixing SnO_2 powder with colloidal form of noble metal ($\approx$3 nm diameter) (colloid method) [79]; and
(3) chemically bonding noble metal complexes such as $PdCl_4^{2-}$ with surface hydroxyls of SnO_2 in solution (fixation method) [80].

The Pd-loaded SnO_2 sensor, for example, shows far larger sensitivity than an unloaded sensor at an operating temperature $<250^{\circ}$C. Higher sensitivity is achieved in the order: fixation > colloid > impregnation method [76]. Catalysts play two important roles:

(1) increase the surface concentration of adsorbed O^- or O_2^- (chemical effect)
(2) pin the Fermi energy of the support at the surface state (electronic effect)

The former can be achieved through the "spill-over" mechanism by which oxygen molecules are dissociated on the catalyst into atoms which are then spilled over onto the support. This is an especially dominant mechanism for the Pt catalyst [81, 82]. The spillover oxygen migrates to the intergranular contact to affect the resistance of the sensor according to Equation 64.

With respect to the electronic effect, from Equation 26, Fermi energy pinning occurs when surface states associated with the catalyst are present in concentrations exceeding 10^{12} cm^{-3}. A fine dispersion of the catalyst pins the Fermi energy of the semiconductor support at the Fermi energy of the catalyst, which varies with the adsorption of gas species according to [83, 84]

$$\Delta\Phi = -\mu N_s \theta/\varepsilon_0 \tag{70}$$

where μ, N_S, θ and ε_0 are the dipole moment of the adsorbed species, the total density of adsorption sites, the fractional coverage, and the dielectric permittivity of free space. Therefore varying the work function of the catalyst with adsorption can change the amount of band bending at the intergranular contacts, and accordingly, the resistance change of the ceramic can be written as

$$\Delta G = G_O \exp\left[-\Delta\left(E_C^S - E_F\right)/kT\right] \tag{71}$$

where, E_C^S and E_F are the surface conduction band energy of the semiconductor and the Fermi level of the catalyst, respectively. As the concentration of adsorbed oxygen on the surface of catalyst increases, the Fermi level of the catalyst and of the supporting semiconductor in contact with the catalyst are correspondingly lowered. This gives rise to a high surface barrier at the intergranular contacts in the same way that a high barrier is obtained with a high concentration of adsorbed oxygen on the semiconductor. In other words, oxygen adsorption on the catalyst removes electrons from the catalyst, which in turn draws electrons from the supporting semiconductor to produce an electron-depleted layer underneath. Because the width of the space charge layer at catalyst/oxide contacts is about 100 nm for typical bulk concentrations of oxygen vacancies of the order of 10^{16}cm^{-3} in SnO_2, the catalyst must be dispersed such that the average distance between catalysts becomes less than about 50 nm for the complete coverage of the space charge layer at the surface.

Ag and Pd are the typical catalysts of this type, which form stable oxides of Ag_2O and PdO at low temperatures in oxidizing atmospheres while they are easily reduced to metals in the presence of inflammable gases [85]. From XPS measurements, Yamazoe [86] and Gonzalez-Elipe [87, 88] observed a work function shift in the Ag-loaded SnO_2 and TiO_2 when they were

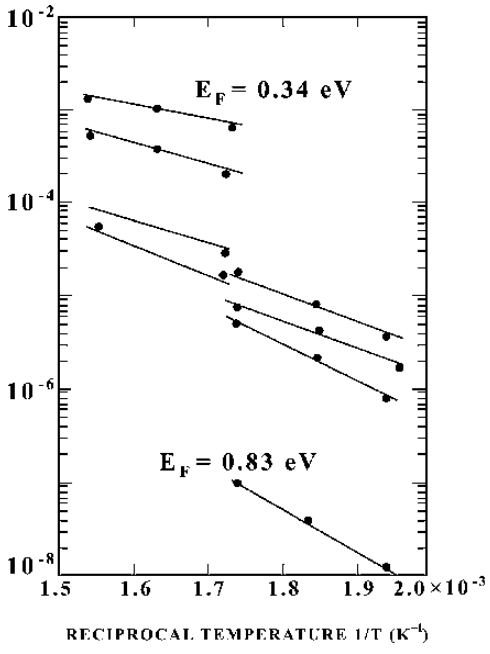

Figure 24 Evaluation of the Fermi level from the Arrhenius plot of a MoO_3 supported on TiO_2 during the reduction process.

exposed to hydrogen gas. The change in Fermi energy of the catalyst (or of the oxide) relative to the surface conduction band edge of the oxide (E_C^S) can be determined from the measurement of conductance as a function of temperature. The slope of an Arrhenius plot according to Equation 71 corresponds to $-(E_C^S - E_F)/k$, determining the barrier height for conduction. Morrison [89] evaluated the Fermi energy change of MoO_3 catalyst on TiO_2 support from the temperature dependence of conductance as shown in Fig. 24. The catalyst was exposed to pulses of the reducing gas (propylene) by which MoO_3 was reduced, which raised its Fermi energy from 0.83 eV to 0.34 eV.

However, PdO is readily formed at a comparatively low temperature of ≈470 K and diffuses into the SnO_2 subsurface at 670 K to act as an acceptor, which destroys the Schottky contact and shows ohmic behavior [90]. The same is observed for Pt/TiO_2 contacts where Schottky behavior is observed at low temperatures, but changes into ohmic contacts upon treatment at high temperature and high oxygen pressure due to the formation of donor defects by the in-diffusion of Pt^{2+} and Pt^{4+}.

4.2. Sensitive and selective design

The fact that a single oxide such as SnO_2 can be used as a base material for the detection of a variety of gases seems to suggest an unlimited potential for oxide based gas sensors. There are, however, at least three issues in the design and response of gas sensors referred to as "3S" that stands for sensitivity, selectivity (or cross-sensitivity) and stability (or aging). Sometimes speed (response time) is included to call it "4S."

4.2.1. Sensitivity

The sensitivity defined as the ratio of the resistance of the sensing element in air to that in the target gas, R_a/R_g, arises from the consumption of negatively charged oxygen adsorbates at or near the inter-grain contacts by the combustible gas. In other words, the sensitivity of a semiconductor gas sensor is a function of the steady state surface coverage of oxygen adsorbate relative to that in air. The lower the surface coverage, relative to that in air, the higher the sensitivity. A sensor with a porous structure shows maximum sensitivity at a certain temperature depending on the gas species to be detected because of these factors:

(1) temperature-dependent equilibrium coverage of oxygen adsorbate in air (adsorption rate of oxygen),
(2) temperature-dependent equilibrium and time constant of the catalytic reaction between the oxygen adsorbate and the target gas (catalytic activity of sensing element) and
(3) permeability of oxygen and the target gas through the porous medium (diffusivity of gases).

At low temperatures, where the equilibrium coverage of the oxygen adsorbate in air [(1)] is high, the catalytic reaction rate of the gas species to be detected with the surface oxygen [(2)] is so low that the sensitivity is negligible. On the other hand, at high temperatures, where the rate of removal of oxygen adsorbate becomes high due to the vigorous catalytic reaction [(2)], the equilibrium coverage of oxygen in air [(1)] is so low that the sensitivity remains low. At intermediate temperatures, a maximum sensitivity appears as shown in Fig. 25a

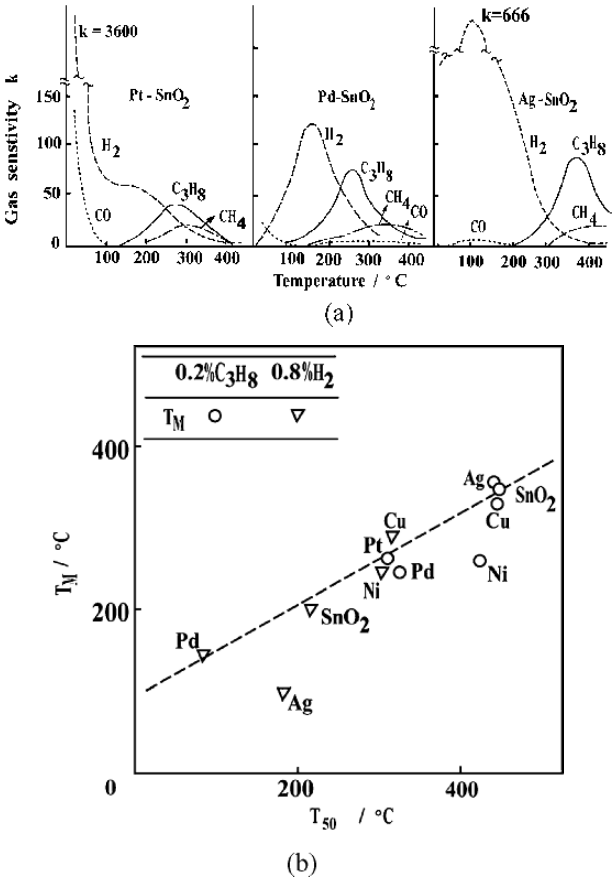

Figure 25 (a) Sensitivity maxima appearing at different temperatures in various SnO_2-based sensing elements for inflammable gas species such as H_2, CO, C_2H_8 and CH_4. (b) Variation of T_M with T_{50} (after ref. 91).

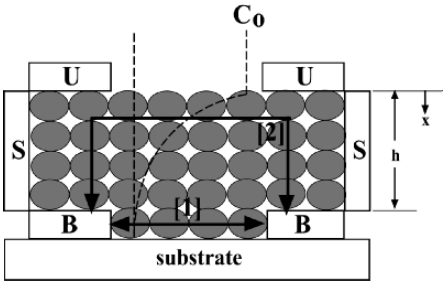

Figure 26 Concentration profile of gas species across the thickness for a thick porous film. Electrodes can be placed on top, at the bottom or on the side of the sensing layer. S: side electrode B: bottom electrode U: upper electrode.

for various reducing gases. Furthermore, since the oxygen consumption related to the conversion of the target gas proceeds at lower temperatures with increasing catalytic activity, the temperature where maximum sensitivity occurs (T_M) is expected to be inversely proportional to the catalytic activity, i.e., the higher the catalytic activity, the lower the sensitivity maximum temperature (T_M). The degree of catalytic activity can be evaluated by the temperature (T_{50}) at which the conversion of the target gas into oxidized species attains 50% in passing through a catalytic membrane. The smaller the T_{50}, the higher the catalytic activity. Accordingly, T_M shows a linear dependence on T_{50} measured from various catalytic activities of sensing materials as shown in Fig. 25b.

In a porous medium, the effective diffusivity of the gas species (D') may be significantly lowered compared to its diffusivity in the ambient, $D^O(D' = 10^{-2}$–$10^{-3}D^O)$. In addition, the gas is consumed during the diffusion across the thick porous layer at a rate of kC_i, which determines the amount of permeation of the target gas [(3)] toward the active surface. Thus a gradient in the gas concentration is usually established across the thick porous film as schematically shown in Fig. 26 which, hence, affects the sensitivity. The concentration profile of the gas species in the film can be obtained by solving the general diffusion equation [92, 93]

$$\frac{\partial C_i}{\partial t} = D_i' \frac{\partial^2 C_i}{\partial x^2} - kC_i \tag{72}$$

where k is the rate constant for the consumption reaction on the surface of the sensing material. At steady state ($\frac{\partial C_i}{\partial t} = 0$), Equation 72 can be solved under the following boundary conditions:

$$C_i = C_i^O \quad \text{at } x = h \quad \text{and} \quad dC_i/dx = 0 \quad \text{at } x = 0$$

to give the concentration of species i as a function of the depth in the sensing layer (x) as

$$\frac{C_i}{C_i^O} = \frac{\cosh[(x/h)(kh^2/D_i')^{1/2}]}{\cosh(kh^2/D_i')^{1/2}} \tag{73}$$

If the conductivity of the sensing material has a relationship with gas concentration according to $\sigma = \sigma_0 + \sigma_1 C_i^\beta$, where σ_0 and β are constants, and the conductance is measured between electrodes placed on the sides (S), the total conductance of the thick film sensor can be obtained by integrating the parallel connection of partial conductance of $\frac{hw}{l}\sigma dx$

$$G = \frac{hw}{l}\left[\sigma_O + \sigma_1 (C_i^O)^\beta \int_0^1 \left[\frac{\cosh[(x/h)(kh^2/D_i')^{1/2}]}{\cosh(kh^2/D_i')^{1/2}}\right]^\beta d\left(\frac{x}{h}\right)\right] \tag{74}$$

where l and w are the length between the electrodes and the thickness of the sensing layer, respectively. Equation 74 can be simplified as

$$G = \frac{hw}{l}\sigma_O + \frac{h^* w}{l}\sigma_1 (C_i^O)^\beta \tag{75a}$$

or

$$G = \frac{hw}{l}\left[\sigma_O + \frac{h^*}{h}\sigma_1 (C_i^O)^\beta\right] \tag{75b}$$

where $\frac{h^*}{h} = \int_0^1 [\frac{\cosh[(x/h)(kh^2/D_i')^{1/2}]}{\cosh(kh^2/D_i')^{1/2}}]^\beta d(\frac{x}{h})$ holds.

The effects of the film thickness on the sensitivity for a given gas component or a given catalytic activity of the material can be evaluated from Equation 75b. The following two extreme cases can be distinguished:

(1) For a very thick film ($h \gg h^*$), $G \approx \frac{hw}{l}\sigma_0$ and no detectable sensitivity can be obtained

(2) For a film with thickness comparable to h^*, $G \approx \frac{hw}{l}[\sigma_O + \sigma_1 (C_i^O)^\beta]$ and an optimum sensitivity can be obtained.

In the case of bottom electrode (B) in Fig. 26, the conductance is determined via either path [1] or path [2], whichever provides the lower resistance channel. This depends on the distance of the electrode-gap and the thickness of the film for a given reactivity of the sensing material. For a narrow gap, the sensitivity most likely comes from the interaction of the gas with the sensing material that resides in the gap between the electrodes. For a wide-gap-sensor, path [1] competes with path [2] such that the reactivity and the thickness of the film affect the sensitivity simultaneously. In summary, if a sensing element is highly active ($h^* \approx 0$), the target gas is almost completely oxidized at the outer region and only a trace amount of the gas species can reach the innermost region where the electrodes are located, leading to a very low sensitivity. On the other hand, if the element has a moderate activity ($h \approx h^*$), a considerable amount of gas species can permeate into the innermost region, giving rise to a high sensitivity. On the contrary, the sensor having a negligible activity again exhibits a lower sensitivity because of the low consumption of oxygen adsorbate at the innermost region in spite of the almost complete permeation of the gas. In this case, the low sensitivity results from the low value of the exponent β in an inactive substrate. The dependence of the permeability of the gas on the activity of the element is schematically shown in Fig. 27 for the bottom electrode structure.

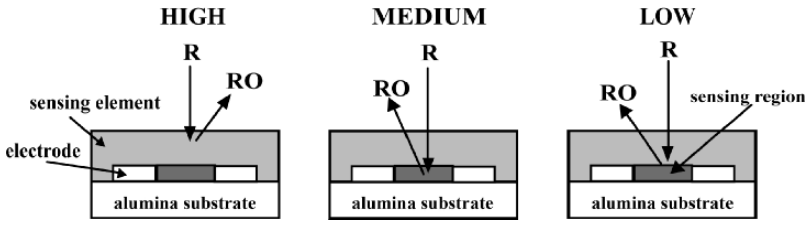

Figure 27 Schematic pictures of gas permeability with different reactivity (high, medium and low) of sensing elements (after ref. 94) R: reducing gas RO: oxidized gas.

4.2.2. Selectivity

The need for high selectivity stems from the fact that the adsorption and the catalytic reaction of species other than the target gas leads to cross-sensitivity. There is a considerable effort to resolve this cross-sensitivity issue. The common approaches for improving selectivity are: (i) adopting a suitable electrode-configuration and thickness of the sensing layer which enables the discrimination of various interfering effects by active gases, (ii) addition of suitable catalysts and/or dopants which shifts the sensitivity maximum towards the target gas and (iii) selection of an optimum operation temperature where the chosen gas is most active. Other approaches include [95]:

- development of new base oxides other than the traditional oxides such as ZnO, SnO_2 and TiO_2;
- use of impedance (frequency modulation) instead of dc resistance measurements;
- use of filtration membrane or multi-layer sensors for selective adsorption or reaction; and
- use of arrays of partially sensitive sensors in conjunction with pattern recognition and multi-component analysis.

The relative measure of the sensitivity and the selectivity would be dependent on the geometrical structure of the electrodes such as:

(1) the position of the electrode
(2) the distance of the electrode gap relative to the thickness of the sensing layer.

The electrodes can be placed on the top surface, or bottom surface, or at the sides as shown in Fig. 28a and their configurations can be chosen as planar, or interdigitized, or micro-contact probe (Fig. 28b). Among them, interdigitated or parallel two-probe with planar configuration is commonly used in practice.

In general, when electrodes are placed on the top or the sides, a higher sensitivity can be obtained than for bottom electrodes because of the effectiveness of surface catalytic reaction of gas species. However, electrodes placed on the bottom are more beneficial in achieving selectivity. For instance, the bottom electrodes with a small gap allow a poorly reactive gas to be detected in the presence of a highly reactive gas because the highly reactive gas effect is removed during the in-diffusion through the sensing layer while less reactive gas remains intact. On the other hand, if the bottom electrodes have a large gap compared to the thickness

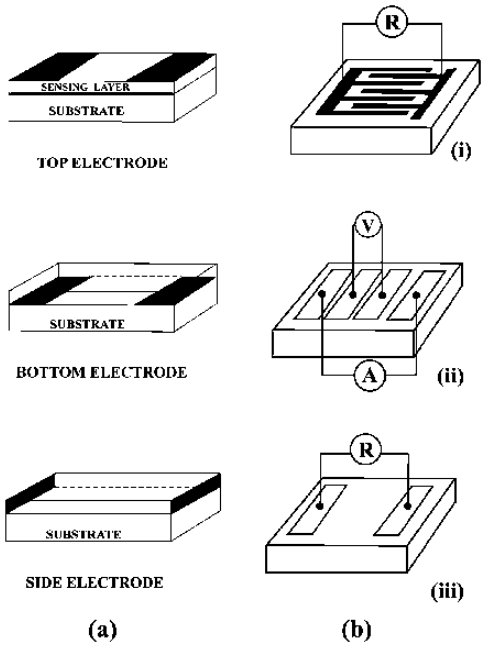

Figure 28 (a) Various positions of electrodes used in the construction of the sensor (b) Various configurations of electrodes used in the construction of the sensor ([i]: interdigitized, [ii]: 4 point micro-contact and [iii]: planar).

of the sensor, the highly reactive gas can be detected in the presence of a poorly reactive gas because the conducting channel is formed through the surface region that is most affected by the reactive gas [96]. For example, Komori [97] achieved the measurement of methane in the presence of more reactive gases such as hydrogen, CO and ethanol by utilizing a sensing layer thicker than the reaction depth for the more reactive gases ($h^* \approx 0$) but smaller than that for methane ($h^* \approx h$).

One of the most effective and positive ways of ensuring selectivity in semiconductor gas sensors is the use of physical or catalytic chemical filters on top of the sensing layer. These filters are highly permeable to the target gas but prevent, physically or chemically, interfering gases from reaching the sensing layer. Examples of physical filters are: a dense SiO_2 layer deposited on a Ga_2O_3 thin film sensing material [98] and 'hot Pt wire' covered with tin oxide powder [99] by sputtering or chemical vapor deposition (CVD). It is particularly efficient to implement hydrogen selectivity because the dense layer acts as a molecular sieve to prevent all other gases except hydrogen with the smallest molecular diameter, from reaching the sensing element. Similarly, chemical filters can permit the target gas to penetrate to the sensor surface but other

gases are removed by the catalytic chemical reaction in the filter. A porous structured Ga_2O_3 filter [100] deposited by screen-printing onto a Ga_2O_3 thin film can eliminate the cross-sensitivity to ethanol such that the selective detection of methane becomes possible in the presence of ethanol, whereas a Nb_2O_5 filter [101] on tin oxide suppresses the cross-sensitivity to hydrocarbons such as propane to detect ethanol selectively.

In addition, the selectivity also depends on the materials and the method of electrode fabrication. For example, a gold electrode provides better selectivity than a Pt electrode, and if a sputtered gold electrode is used, better sensitivity can be obtained than for screen-printed gold [102]. The reason for these phenomena is not completely known but it is closely related with the catalytic activity of the electrode.

4.2.3. Stability

In contrast to the selectivity and sensitivity issues, the problem of stability is rarely addressed in the literature. This does not mean that the stability issue has less impact on the usefulness of a gas sensor. Rather, stability is an engineering issue often addressed at the prototyping and manufacturing stages, and is difficult to resolve mostly due to a lack of precise knowledge of the underlying physical and chemical processes. The problem of stability may be associated with the facts that:

(1) a surface conductive sensor readily suffers from surface contamination due to its rather low operating temperature of 100–450°C;

(2) an oxide-based sensor consists of an incompletely sintered body in which the intergranular contacts are not identical; and

(3) changes can occur from thermal expansion coefficient mismatch and/or interfacial reactions at the metal electrode/ceramic interface.

First, the working temperature of most of the surface conductive sensors are not high enough to completely burn out organic deposits or desorb certain adsorbates, which inhibits the adsorption of oxygen and the target gas in repeated operations. This leads to long-term instability over time and requires frequent cleaning procedures at high temperatures. Secondly, the electrical response from the sensor can be considered as a collective phenomenon based on the existing distribution of the contact areas and barrier heights. In other words, a Schottky barrier gas sensor can be considered as an assembly of micro-sensors at the intergranular contacts. For long-term operation at relatively high working temperatures, this distribution may change with time due to changes in the microstructure and/or segregation of impurities, which results in aging or long-term drift. Thirdly, the mechanical and the chemical compatibility are destroyed at the electrode/sensor interface due to frequent thermal cycling at high temperatures. For instance, silver electrodes are prone to aging because silver can easily move under the electric field imposed on the electrode at the operating temperature above 300°C.

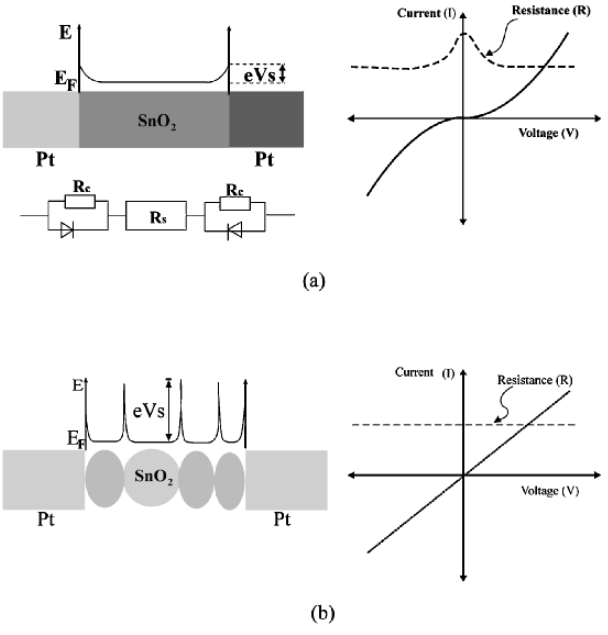

Figure 29 Schematic energy band structure for (a) thin film and (b) thick film sensors with their equivalent circuit and current-voltage response. (after ref. 105).

In general, the metal/ceramic contacts show a non-ohmic behavior because of the work function difference of the ceramic and the metal. For example, a Schottky type barrier is formed at the Pt/SnO_2 interface [103–106]. Hence when the electrical response is measured for the contact-controlled structures with a Pt electrode on sintered SnO_2 sensors with a thickness, $h > h^*$, the contact property plays a dominant role in the current-voltage response to give a current dependent or bias voltage dependent resistance as shown in Fig. 29a. However, it is alleviated in porous thick film structure which is connected in series with a large number of Schottky grain-grain contacts with comparable resistance as shown in Fig. 29b.

4.3. Thermal design

In practice, chemoresistive gas sensors based on SnO_2 are operated around 350°C to avoid the cross-sensitivity from humidity. Hence they are usually equipped with a heater printed on the backside of the alumina substrate for thin or thick film devices or heating elements are positioned outside the bulk type devices. The power dissipated at the heater can be expressed in terms of the resistance, R, and the operating voltage, V, of the heating material, expressed as

$$P = \frac{V^2}{R} \tag{76}$$

Therefore, there are two ways to reduce the power consumption of the sensor:

(1) increasing the resistance of the heater for a given operating voltage, or

(2) lowering the operating voltage for a given resistance of the heater.

Initially, wound Pt alloy wire was used in the bulk sintered SnO_2 sensor as a heating element, which had a resistance of a few decades of ohms (Ω). Soon this was replaced by Pt paste on an alumina substrate in the thick film device with practically the same magnitude of resistance but much smaller size. However, the power has been dramatically reduced from 800 mW to as low as 200 mW by changing the operating voltage from 5 V to battery-operated 2 V accompanying its dimensional reduction. Size reduction leads to low power consumption to attain the same operation temperature. The power can also be reduced, without changing the operating voltage, by adopting high resistance materials such as RuO_2 ink with which heaters of several hundreds ohm (Ω) can be easily made. Furthermore, the resistance of RuO_2 ink is insensitive to the change in temperature while the resistance of Pt paste approximately doubles when it reaches the operating temperature of 350–400°C.

However there is a lower limit to which power can be reduced due to the conduction loss through the connecting wires with the external circuitry in addition to the radiation and the convection loss to the outside. For example, Au wire of 25 μm diameter gives rise to about 30 mW power dissipation per line at an operating temperature of 400°C. Therefore, the power to be supplied for maintaining an operating temperature has to be at least more than 120 mW, if four lines are connected to the external circuit, which is common for most of the surface conductive gas sensors.

4.4. Measurement and calibration

Generally, a voltage-dividing circuit is used to detect the resistance of the sensor as shown in the inset of Fig. 30. The output voltage becomes

$$V_{\text{out}} = \frac{R_{\text{L}}}{R_{\text{L}} + R_{\text{S}}} V_{\text{C}} \tag{77}$$

where R_{L} and R_{S} are the load resistance and the sensor resistance, respectively, and V_{C} is the operating voltage of the sensor. Graphically, output voltage can be drawn as a function of $\log R_{\text{S}}/R_{\text{L}}$ as shown in Fig. 30b for $V_{\text{C}} = 5$ V. When $0.1 < R_{\text{S}}/R_{\text{L}} < 10$, the output voltage exhibits its most sensitive response to a change in R_{S}. However, outside this region, the change in R_{S} cannot attribute to the output voltage change as sensitive as within the specified range. Therefore, sensitivity of more than 100 is unnecessary for achieving acceptable resolution of detection. Because the resistance of the sensor usually decreases upon exposure to the reducing gas, a load resistor having a lower resistance than that of sensor is recommended. According to Fig. 30, in order for a sensor to operate in the sensitive region, R_{L} must be smaller than ten times of R_{S} at the most, which sets the upper limit of the resistance of the sensing material.

The lower limit of the sensor resistance is determined by the resistance change caused by the self-heating of the sensing element. Fig. 31 shows the voltage across the sensing material with changing sensing current in air and 2000 ppm CH_4, where the slope corresponds to the resistance of the sensing element. The sensing material shows a pure ohmic linear behavior until it reaches 10 mW above which the resistance decreases due to self-heating by the sensing current. Therefore, the maximum power dissipation of the circuit, which occurs at $R_{\text{S}} = R_{\text{L}}$, must be smaller than 10 mW.

$$P_{\max} = \frac{V_{\text{C}}^2}{4R_{\text{S}}} < 10 \text{ mW} \tag{78}$$

In other words, R_{S} must be smaller than $V_{\text{C}}^2/0.04$ (Ω). For most modern sensors, the operating voltage V_{C} is around 5 V, though some are designed for 2 V for battery operation. Hence, the lower limit for the resistance of the sensing material is set at 0.6 K Ω and 0.1 K Ω for 5 V and 2 V, respectively. These values are much smaller than that for doped SnO_2 devices.

5. Applications

5.1. Methane sensor

Around the world, natural gas (which is largely methane) is being used in domestic, commercial and industrial premises. Reliable methane sensors are needed for these applications, especially as a domestic gas alarm system, which is mandated by law in some countries. Methane is rather stable compared to ethanol,

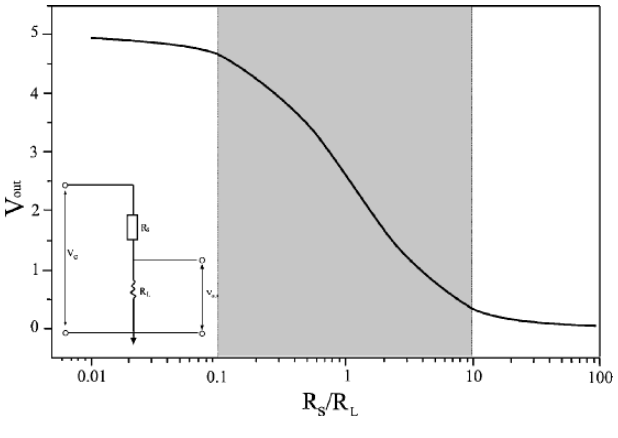

Figure 30 (a) Circuit for the measurement of gas (R_{S}: sensor resistance R_{L}: load resistance); (b) Output voltage as a function of $R_{\text{S}}/R_{\text{L}}$ (after ref. 101).

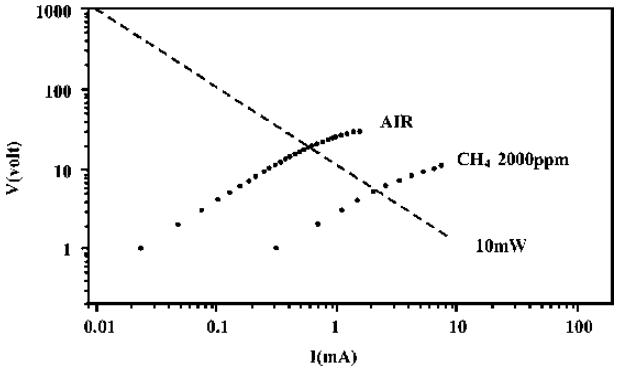

Figure 31 The change in the resistance due to self-heating of sensing element.

which is often produced as a by-product of cooking or food processing and can cause a false alarm. Hence, the selectivity of a methane sensor over ethanol is important in the domestic application. In addition, the application requires long-term stability or minimal aging due to any degradation in the sensor material, power variation in the circuit, temperature fluctuation and humidity changes.

The commercial devices set their alarm operation to a certain range of methane concentration within which an alarm must operate (Table IV). The upper limit is well below an explosive level but the lower limit is high enough to avoid most false alarms from interfering gases. For example, the instrument which must give an alarm between 2500 and 10000 ppm for satisfactory operation (British Standard 7348) is usually set to about 3500–4000 ppm in actual operation. This leaves a considerable room for variation resulting from power and temperature fluctuation, humidity change and degradation of the sensor.

Furthermore, because the semiconductor gas sensors are usually operated at high temperature above 350°C, the device must be packaged to avoid explosion even at a methane concentration well above the lower explosion limit (LEL). Stainless gauze is normally provided to limit the explosive gas supply from outside.

5.2. Carbon monoxide sensor

Highly toxic carbon monoxide gas can build up in a confined space, either directly from coal gas leaks or via the incomplete combustion of methane. Hence in many applications, warnings for toxic levels of carbon monoxide are required in addition to a methane alarm. When carbon monoxide is inhaled, it is picked up by the blood more readily than oxygen, forming carboxyhemoglobin. Below 10% carboxyhemoglobin which corresponds to 60 ppm CO in the ambient, the physiological effect is negligible. Hence, for exposure over several hours, 50 ppm CO is set to a tolerance limit value (TLV) level in Europe, Japan and Korea and 35 ppm in the US.

For a maximum selectivity to carbon monoxide, the SnO_2-based sensor must be operated below 100°C, where the response is slow and miscellaneous gas species are easily adsorbed to interfere with sensor operations. Therefore, the sensor is heated sequentially to a high purging temperature of about 300°C, followed by a low operating temperature of about 100°C as shown in Fig. 32. The conductivity of the sensing material is measured at the end of each operating period to indicate CO concentration in air. In general, a material that is sensitive to carbon monoxide is also sensitive to ethanol such that an activated charcoal filter is commonly incorporated in the package to filter out any interfering alcohol vapor.

CISM (Center for Industrial Sensors and Measurements) researchers have designed a new type of selective CO sensor based on *p-n* heterojunctions of anatase (*n*) and rutile (*p*) using TiO_2 as the base material [108]. Combination of anatase and rutile phases in the appropriate proportions leads to a sensor selective to CO as shown in Fig. 33. These types of composite sensors have

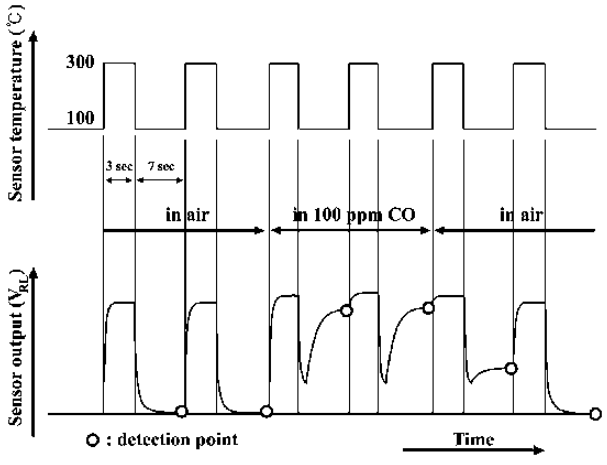

Figure 32 Cyclic heating in the detection of CO. Detection is made at the end of the heating cycle (open circle). Source: FIS technical manual in http://www.fisinc.co.jp

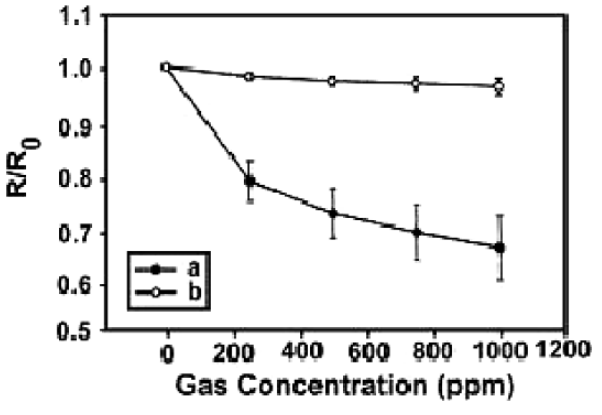

Figure 33 Sensing behavior of a *p-n* composite sensor (75% rutile and 25% anatase TiO_2) at 600°C in 5%O_2 (a: CO and b: CH_4). R_o is the resistance in the absence of the sensing gas (after ref. 108).

tremendous potential because by varying the mixing ratio of the *n* and *p* phases one can create a wide range of sensor arrays including the possibility of designing selective CO and/or hydrocarbon sensors.

5.3. Alcohol sensor

Detection of alcohol concentration in the brain is important for safety on the road as well as in the workplace. Conveniently, blood alcohol concentration (BAC), defined as the percentage of alcohol in the blood, is used to assess the alcohol level in the brain tissue as a measure of impairment from alcohol poisoning. Most people show measurable mental impairment at about 0.05% BAC. Above this level, the ability to operate an automobile deteriorates progressively with increased blood alcohol level. For the average person, unconsciousness results about a BAC of 0.4%. Above 0.5% BAC, basic body functions such as breathing or the beating action of the heart can be depressed leading to death. Major symptoms occurring in a person who is intoxicated by alcohol are listed in Table V.

One of the convenient and non-invasive ways of obtaining BAC is to measure the alcohol concentration in the deep lung breath. Approximately 0.01% BAC corresponds to 16 ppm alcohol in the breath stream (BrAC is often used to indicate that the measurement is a breath

TABLE IV Specifications of domestic gas alarm standards [107]

	Inspection standards for town gas leakage alarm; Japan Gas Appliances Inspection Association, Japan	Specification for the detection of combustible gases in domestic premises; British standard BS 7348, UK	Residential gas detectors. UL 1484 standard for safety; Underwriters Lab. Inc., USA
Alarm concentration in standard atmosphere	1/200–1/4 of LEL. Methane: 0.1–1.25%. (1000–12,500 ppm)	5–20% of LEL. Methane: 0.25–1.0%. (2500–10,000 ppm) Not specified precisely	Less than 25% of LEL; natural gas: 0.95% (the LEL of N.G. specified as 3.8% in this standard)
Fluctuation of alarm conc. by atmospheric temp. and humidity	−10°C–50°C; alarm as above. 35–40°C, >85% RH; alarm as above 50°C; clear of false alarms by miscellaneous gases. Fluctuation of ±10%; alarm as above	The above is to be maintained from 15°C, 35% RH to 25°C, 60% RH. Fluctuation of +10% and −15% of 240 V; alarm as above	Fluctuating upper limit: $U = (K + I)/2$; K: 25% of LEL; I; Initial alarm. conc. Alarm as above, under all the following conditions: 0°C, 30% RH. ∼49°C, 50% RH; 30°C, 0% ∼ 90% RH; and at 42°C, 95% RH Fluctuation of +10% and −15%; as above
Change in alarm conc. by supply voltage fluctuations	After one month or more storage with and without energizing; alarm as above and clear of false alarms by miscellaneous gases;	After 3 months being subjected to 5% and 20% of LEL once a week; alarm as above	Alarm as above during three months observation being subjected to temperature change, gas flow velocity change, etc.
Long-term stability	Durability for over 5 years	Not specified	Not specified
Response speed to alarm	At 1/4 LEL (methane 1.25%); alarm within 20 sec	At 25% of LEL (methane 1.25%); Alarm within 30 sec	Not specified
False alarm by miscellaneous gases explosion proofing of sensor housing	For ethanol of 0.1% or less at 38–40°C, >85% RH; no alarm. Proofed with double stainless steel gauze as specified or with more strict flame arrester	Same as Japanese specification; no ignition for 10 times sparking in a mixture of 28 ± 1 & hydrogen in air	No ignition for 10 min energizing with 10% supply voltage in 8.3% natural gas

measurement) and BAC values thereafter increase proportional to the breath alcohol concentration. A variety of methods such as photospectroscopy, gas chromatography, Infrared spectroscopy, semiconductor sensor and fuel cell have been adopted to test a breath sample for alcohol. Among them, the alcohol breath analyzer using a semiconductor sensor offers significant merits such as low cost, portability, high accuracy and rapidity in consecutive testing. Some of the commercial portable devices are shown in Fig. 34. However, these devices have inherent interference effects from acetone present in the breath of diabetics and from cigarette smoke. They also need frequent calibration for which a breath alcohol sample simulator (BASS) is used to provide an alcohol-in-air test sample with known alcohol level at 34°C [109].

Another useful application of alcohol detection is in the area of automatic control of fermentation processes, especially when alcoholic fermentation must be avoided. One example is the fabrication of beer yeast, where the ethanol concentration in the solution must be maintained below 0.1%. The sensor tracks the ethanol level in the reactor to determine the modification of the reaction parameters in the reactor before it reaches the threshold value.

TABLE V Various human symptoms according to the blood alcohol concentration (BAC)

Blood alcohol concentration (BAC)	Symptoms
>0.05%	Measurable mental impairment
>0.10%	Unsteady walk
>0.15%	Slurred speech
>0.40%	Unconsciousness
>0.50%	Difficulty in breathing, heart failure, death

6. Sensor arrays and pattern recognition

Another active area of gas sensor research is the use of pattern recognition techniques to obtain selectivity from sensors that may otherwise appear non-selective. Some of the approaches are as simple as monitoring the sensor response over a range of temperature, while others involve the use of artificial neural networks.

Takada had developed an approach for testing and extracting a selective response from a single gas sensor [110]. By looking at both the resistance change and the temperature change of a sensor when exposed to a gas, a 2D map was developed of the sensor response to a number of gas concentrations. An example of one of these maps is shown in Fig. 35. Each gas has its own response curve over a range of concentration, and the curves do not intersect. From this map, the concentration and identity of an unknown gas (assuming, of course, that it is one of the gases that has been previously tested) can be determined. The advantage of the method is that if the concentration of the unknown gas changes during the course of the measurement, it will still fall on the response curve, making unique identification possible [110].

Figure 34 Various alcohol breath analyzers using a semiconductor sensor (adopted from http://www.dui.com, http://www.intox.com, and http://www.lifeloc.com).

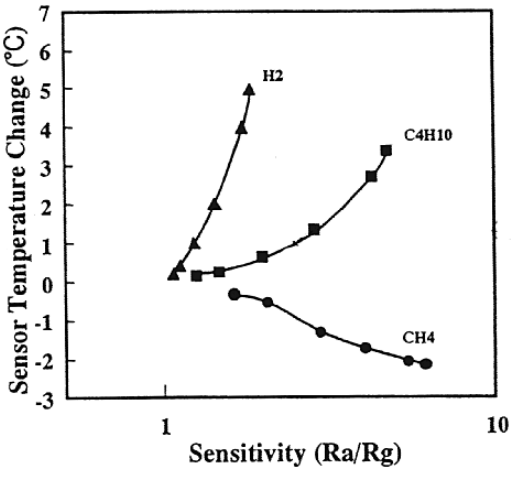

Figure 35 Map of sensitivity vs. temperature change for selective detection of gases (after ref. 110).

Other approaches have used dynamic temperature programming to find patterns in the response of a sensor to particular analytes [111]. Temperature pulses are applied to the sensing film, and the response of the sensor is followed with time. The conductance signature for each gas to this applied temperature pulse is unique, as shown in Fig. 36 [111].

Pattern recognition and artificial neural network methodologies have also been utilized for making selective sensor arrays [112]. Chambon *et al*. developed a pattern recognition approach using 4 different metal oxide sensors [113]. They used the response of each sensor for a number of gas concentration, to calculate features that, though not able to determine gas quantity, could identify the gas. Two-dimensional plots of the feature vectors were used to show how the signals from the different gases clustered together. This methodology, a modification of principal component analysis, accurately identified the two test gases, NH_3 and CO [112]. Hong *et al*. used both principal component analysis and artificial neural networks to classify and identify different flavor compounds [114]. The principal component analysis resulted in the overlap of signals for two of the compounds, while the artificial neural network correctly identified the flavor samples 93% of the time [114].

To extract information from a sensor array, software algorithms are needed to identify distinct features in the multiplicity of sensor data. As a first approach, Fulkerson [115] trained a simple neural network, using Gaussian basis functions, to interpolate the sensor response based on relatively sparse gas composition data. His results clearly illustrated that although the fit goes through the data points, nonphysical oscillations of the sensor response occur for regions outside the range of the training gas concentrations. This illustrates a problem with neural nets, namely, they do not extrapolate well outside of the data set for which they are trained. Relying on theoretical understanding of the sensing mechanism combined with experimental data, Fulkerson *et al*. [116] developed an alternative knowledge-based kernel regression approach based on support vector machine (SVM) theory. They demonstrated that the SVM modeling provides a much better and more reasonable prediction for larger values of the gas concentrations.

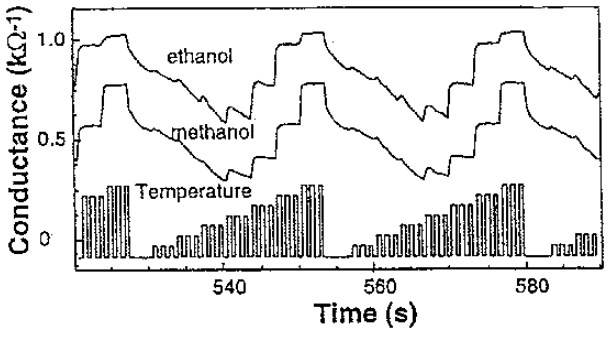

Figure 36 Response of sensors to different gases with pulsed temperature operation (adapted from reference 111).

7. Future trends

As pointed out in the previous sections, selectivity and stability are the major issues limiting widespread applications and further development of oxide based sensors. Current efforts to resolve these issues tend to integrate results obtained from both empirical and basic science approaches, and to focus on various stages of sensor development, including development of new material systems for high temperature applications, sensor fabrication and manufacturing techniques, and neural-network-based *smart* sensor arrays with signal conditioning and filtration. Also, due to the complexity

involved in sensor development, the research trend is moving more toward multi-disciplinary collaborative approaches.

7.1. Development of new sensor materials

Typical gas sensors often involve a complex mix of different materials including catalysts. However, not much is known about the relation between sensing mechanisms and microstructure, which is necessary to exploit the full potential of existing materials or to find improved sensor systems, as well as to control the stability of fabricated devices. Detailed characterization ranging from electron microscopy to surface analytical techniques is needed for establishing structure-property relationships.

Very little work has been done in the area of modeling and simulation of ceramic gas sensors, particularly modeling of sensor arrays [115–118]. The difficulty arises since development and integration of modeling at different length scales is necessary to describe the multitude of phenomena occurring in various types of sensors. The fundamental chemical reactions and electron transport through metal oxide surfaces and bulk regions involve events on the atomic scale. Conduction through the poorly sintered microstructure of the ceramic device involves phenomena at the granular or mesoscopic scale while the device electrical properties include behavior at the macroscopic level as well. There is a need to combine successful models developed at these different length scales into an integrated framework that can be used to drive new research and guide experimental efforts for designing sensors and sensor arrays with optimized properties [115–118].

Ultra thin or nano-particle films show promise in gas sensor applications because the sensitivity is expected to increase dramatically when the film thickness or particle size becomes comparable to the depletion layer thickness of the material. A challenging issue associated with the development of ultra thin film and nano-structured ceramic sensors is the stability of the nano-scale microstructure against surface grooving, grain growth and coarsening during thermal processing and applications at elevated temperatures. Both experimental and theoretical studies are needed for the kinetics of surface/interface grooving as a function of the ratio of surface/interfacial energy over grain boundary energy, temperature and segregation of impurities on surface/interface/grain boundaries.

7.2. Smart sensors and sensor arrays

There is a trend toward the use of more sophisticated design concepts in the development of new sensor systems, notably the so called smart sensor system, which combines sensing elements and signal processing, conversion and output units. This approach aims at simultaneous or sequential acquisition of more than one type of signal, mainly to resolve the problem of selectivity. This may include the use of more than two electrodes (arrays of electrodes) on a single sensor body, employment of sensor arrays made of many sensors or a multi-layer sensor with a filtering membrane, and applications of artificial intelligence for pattern recognition. In applications, the objective of such an approach may be difficult to achieve, as a sensor array functionality relies not only on the *right* combination or integration of different sensors but also on the stability of individual sensors. Any change or drift in one of the sensors requires a system-wise re-calibration or re-programming of the pattern recognition part. In other words, potential applications of a sensor array system are still going to be determined by the availability of stable and reliable individual sensors.

7.3. Device fabrication and manufacturing

From the device fabrication and manufacturing point of view, besides the issues of poor selectivity and long-term stability, oxide based sensors are also plagued with issues such as poor reproducibility (unit-to-unit consistency) and high power consumption (particularly for gas sensors to maintain a constant operating temperature). Poor reproducibility results from poor control over raw materials and processing conditions including forming, firing and electrode attachment. Most of the current commercial sensor devices are produced either by typical ceramic fabrication (sintered body) or thick film processes. Sensors thus produced often have poor unit-to-unit consistency, and therefore require individual inspection and calibration.

Thin film fabrication process and micromachining, which are based on well-defined IC deposition and etching processes, are expected to improve the reproducibility and possibly lower the power usage besides achieving a mass production capability. Alumina fabricated by low temperature co-fire ceramic technology (green tape technology) provides new opportunities for IC packaging as a high-density, high-reliability, low-cost substrate. Thin film metallization can be accomplished by thermal evaporation, sputtering and chemical vapor deposition on a polished alumina substrate. Patterning of the structure can be done using proven photoresist, chemical etching and lift-off techniques. Green tape and laser cutting techniques can be used together to create three-dimensional structures, which are highly desirable for many sensor and device applications. The conventional ceramic green-tape process produces surface with roughness $\sim 1\ \mu$m, which is relatively rough for thin film metallization with typical thickness of 2000–3000 Å. This would lead to discontinuous metallic film on the ceramic substrate making the electrode unstable. Therefore, mechanical polishing of ceramic substrate prepared via tape-cast is necessary for thin film metallization.

8. Summary

Despite many problems addressed above, the development of oxide-based gas sensors is expected to continue, and the market appears to be promising; the US demand alone for chemical sensors (gas sensors and biosensors) is projected to reach $2.7 billion by 2006

[8]. Several emerging research trends contribute to such a perspective: (i) increased efforts in basic studies in recent years resulting in better understanding of sensing mechanisms; (ii) new and improved materials synthesis and device fabrication techniques; and (iii) developing sensors for more specific or focused applications rather than a generic application targeted at all markets. The last aspect can help to elevate the acceptance level of ceramic sensors and promote further development for specific sensors for use in various environments.

Development of ceramic gas sensors for industrial applications appears to be more challenging. Selectivity and stability issues become even more challenging in a harsh industrial environment with high temperature, high pressure, contaminants and dynamic gas flow. The increasing need for measurement in industrial processes and products, however, shows promise for future growth via innovative scientific and/or engineering approaches. What makes this area exciting for future R&D is that the solution to the engineering and technological problems is closely linked with the fundamental knowledge and understanding yet to be uncovered.

Acknowledgements

Collaboration of Dr. Prabir Dutta and Dr. Bruce Patton on the selective CO sensor and sensor array work is acknowledged. Technical comments from Joe Trimboli and Dr. Ramamoorthy on the manuscript are greatly appreciated.

References

1. E. M. LOGOTHETIS, *Chem. Sens. Techn.* **3** (1991) 89.
2. A. M. AZAD, S. A. AKBAR, S. G. MHAISALKAR, L. D. BIRKEFELD and K. S. GOTO, *J. Electrochem. Soc.* **139** (1992) 3690.
3. N. YAMAZOE and N. MIURA, *Sensors and Actuators* B **20** (1994) 5.
4. S. VISWANATHAN, R. G. REDDY and J. C. MALAS (eds.), "Sensors and Modeling in Materials Processing: Techniques and Applications" (The Minerals, Metals and Materials Society, Warrendale, PA, 1997).
5. N. FUKATSU, N. KURITA, K. KIODE and T. OHASHI, *Solid State Ionics* **113–115** (1998) 219.
6. S. A. AKBAR and P. K. DUTTA, "Ceramic Sensors for Industrial Applications" (Encyclopedia of Materials: Science and Technology, Elsevier, 2001) p. 1080.
7. O. W. BYNUM, D. R. SHERIDAN and J. A. WHITE, *GRI Report 92/0373*, 1992.
8. K. SWIFT, Industrial Sensor Technologies and Market, BCC, Inc. Report, GB-200R, Jan. 2002.
9. H. N. McMURRAY and J. ALBADRAN, *MRS Bulletin* **34** (1999) 55.
10. M. LIU, T. DOL, B. FLIETNER, J. LECHNER and I. EISELE, *Sensors and Actuators* B **18/19** (1994) 678.
11. Y. GURBUZ, W. P. KANG, J. L. DAVIDSON and D. V. KERNS, *ibid.* **56** (1999) 151.
12. W. P. KANG and C. K. KIM, *ibid.* **13/14** (1993) 682.
13. A. SAMMAN, S. GEBREMARIAM, L. RIMAI, X. ZHANG, J. HANGAS and G. W. AUNER, *ibid.* **63** (2000) 91.
14. W. ZHU, *et al.*, *J. Mat. Sci.* (special issue on sensors) (2003).
15. U. KIRNER, B. LEIBOLD, D. FISCHER, K. D. SCHIERBAUM, N. NICOLOSO, W. F. CHU, W. WEPPNER and W. GOPEL, *Sensors and Actuators* B **1** (1990) 103.
16. J. PENNEWEISS and B. HOFFMANN, *Mater. Lett.* **5** (1987) 121.
17. W. J. KAISER and E. M. LOGOTHETIS, SAE Paper No. 830167 (1983).
18. N. H. CHAN and D. M. SMYTH, *J. Electrochem. Soc.* **123** (1976) 1584.
19. P. T. MOSELEY, *Meas. Sci. Technol.* **8** (1997) 223.
20. P. T. MOSELEY and D. E. WILLIAMS, *Polyhedron* **8** (1989) 1615.
21. K. D. SCHIERBAUM, U. K. KIRNER, J. F. GEIGER and W. GÖPEL, *Sensors and Actuators* B **4** (1991) 87.
22. P. W. SELWOOD, "Chemisorption and Magnetization" (Academic Press, New York, 1975).
23. I. LUNDSTROM, in "Chemical Sensor Technology," Vol. 2, edited by T. Seiyama (Elsevier, 1989) p. 1.
24. G. KOROTCHENKOV, V. BRYNZARI and S. DMITRIEV, *Sensors and Actuators* B **54** (1999) 197.
25. J. F. BOYLE and K. A. JONES, *J. Electron. Mater.* **6** (1977) 717.
26. G. HEILAND and D. KOHL, in "Chemical Sensor Technology," Vol. 1, edited by T. Seiyama (Kodansha,Tokyo, 1989) p. 15.
27. M. EGASHIRA, M. NAJASHIMA and S. KAWASUMI, *J. Phys. Chem.* **85** (1981) 4125.
28. Y. TAMAKI, M. NAGAISHI and Y. TERAOKA, *et al.*, *Surf. Sci.* **86** (1979) 335.
29. S. SEMANCIK and D. F. COX, *Sensors and Actuators* **12** (1987) 101.
30. S. G. DAVISON and M. STESLICKA, "Baisic Theory of Surface State" (Oxford Sci. Publications, 1992) p. 61.
31. S. R. MORRISON, "The Chemical Physics of Surfaces," 2nd ed. (1977) p. 135.
32. M. J. MADOU and S. R. MORRISON, "Chemical Sensing with Solid State Devices" (Academic Press, 1988) p. 74.
33. M. IWAMOTO, Y. YODA, N. YAMAZOE and T. SEIYAMA, *J. Phys. Chem.* **82** (1978) 2564.
34. S. C. CHANG, *J. Vac. Sci. Technol.* **17** (1980) 366.
35. S. LENAERTS, J. ROGGEN and G. MAES, *Spectrochimica Acta Part A—Molecular Spectroscopy* **51** (1995) 883.
36. J. P. JOLY, L. GONZALEZ-CRUZ and Y. ARNAUD, *Bulletin de la Sociètè Chimique de France* **1** (1986) 11.
37. B. GILLOT, C. FEY and D. DELAFOSSE, *J. Chem. Physics* **73** (1976) 19.
38. N. YAMAZOE, J. FUCHIGAMI, M. KISHIKAWA and T. SEIYAMA, *Surf. Sci.* **86** (1979) 335.
39. S. C. CHANG, *J. Vac. Sci. Technol.* **17** (1980) 366.
40. J. LUNSFORD, *Catal. Rev.* **8** (1973) 135.
41. H. CHON and J. PAJARES, *J. Catal.* **14** (1969) 257.
42. S. R. MORRISON, *Surface Sci.* **27** (1971) 586.
43. N. BARSAN, M. SCHWEIZER-BERBERICH and W. GOPEL, *Fresenius J. Anal. Chem.* **365** (1999) 287.
44. W. SCHOTTKY, *Ztschr. Phys.* **113** (1939) 367.
45. W. SCHOTTKY and E. SPENKE, *Wiss. Veroffentl. Siemens-Werkon.* **18** (1939) 3.
46. N. F. MOTT, *Proc. Roy. Soc.* A **171** (1939) 27.
47. H. J. ENGELL and K. HAUFFE, *Ztschr. Electrochem.* **56** (1952) 336.
48. P. B. WEISZ, *J. Chem. Phys.* **21** (1953) 1531.
49. TH. WOLKENSTEIN, *J. Chem. Phys. (USSR)* **21** (1947) 1317.
50. *Idem.*, *ibid.* **22** (1948) 311.
51. *Idem.*, *ibid.* **26** (1952) 1462.
52. *Idem.*, *ibid.* **28** (1954) 422.
53. F. F VOLKENSTEIN, "Electron Processes on the Surface of Semiconductors during Chemisorption" (Nauka Publ., Moscow, 1987).
54. TH. WOLKENSTEIN, *J. Chim. Phys.* **54** (1957) 181.
55. *Idem.*, *Advan. Catal.* **12** (1960) 189.
56. W. E. GARNER, *ibid.* **9** (1957) 169.
57. O. V. KRYLOV, S. Z. ROGINSKY and E. A. FOKINA, *Bull. Acad. Sci. USSR, Div. Chem. Sci.* (1957) 422.
58. P. T. MOSELEY and B. C. TOFIELD, "Solid State Gas Sensors" (Adam Hilger, 1987) p. 93.
59. J. F. McALEER, P. T. MOSELEY, J. O. W. NORRIS and D. E. WILLIAMS, *J. Chem. Soc., Faraday Trans.* **1** (83) (1987) 1323.

60. K. D. SCHIERBAUM, U. WEIMAR and W. GÖPEL, *Sensors and Actuators* B **3** (1991) 205.
61. M. NAKAGAWA and H. MITSUDO, *Surf. Sci.* **175** (1986) 157.
62. P. K. CLIFFORD and D. T. TUMA, *Sensors and Actuators* **3** (1983) 233.
63. P. K. CLIFFORD, in Proc. 1st Int. Conf. Chemical Sensors, Fukuoka, Japan (Kodansha, Elsevier, 1983) p. 135.
64. K. D. SCHIERBAUM, U. WEIMAR and W. GÖPEL, *Sensors and Actuators* B **3** (1991) 205.
65. S. STRASSLER and A. REIS, *ibid.* **4** (1983) 465.
66. H. WINDISCHMANN and P. MARK, *J. Electrochem. Soc.* **126** (1979) 627.
67. K. IHOKURA and J. WATSON, "The Stannic Oxide Gas Sensor Principles and Applications" (CRC Press, 1994) p. 55.
68. P. K. CLIFFORD and D. T. TUMA, *Sensors and Actuators* **3** (1983) 233.
69. H. PINK, L. TREITINGER and L. VITE, *Jpn. J. Appl. Phys.* **19** (1980) 513.
70. N. SAVAGE, "Development and Characterization of High-Temperature, Selective, Titania-Based Gas Sensors," Ph.D. thesis, The Ohio State University, Columbus, OH, 2002.
71. Figaro Technical Handbook.
72. K. D. SCHIERBAUM, S. VAIHINGER, W. GÖPEL, H. H. FAN DEN VLEKKERT, B. KLOECK and N. F. DE ROOIJ, *Sensors and Atuators* B **1** (1990) 171.
73. T. M. UEN, K. F. CHEN and Y. S. GOU, *Thin Solid Film* **158** (1988) 69.
74. M. DIGIULIO, G. MICOCCI, R. RELLA, P. SICILIANO and A. TEPORE, *Sensors and Actuators* B **23** (1995) 193.
75. S. S. PARK and J. D. MACKENZIE, *Thin Solid Film* **274** (1996) 154.
76. C. XU, J. TAMAKI, N. MIURA and N. YAMAZOE, *Sensors and Actuators* B **3** (1991) 147.
77. N. YAMAZOE, *ibid.* **5** (1991) 7.
78. S. MATSUSHIMA, T. MAEKAWA, J. TAMAKI, N. MIURA and N. YAMAZOE, *Sensors and Actuators B: Chemical* **9** (1991) 71.
79. Y. NAKAO, *Hyomen* **24** (1986) 413.
80. T. KAJI, H. OONO, T. NAKAHARA, N. YAMAZOE and T. SEIYAMA, *J. Chem. Soc. Jpn.* (1980) 1088.
81. G. E. BATLEY, A. EKSTROM and D. A. JOHNSON, *J. Catal.* **36** (1975) 285.
82. S. R. MORRISON, *Sensors and Actuators* **12** (1987) 425.
83. J. HORIUTI and T. TOYA, in "Soilid State Surface Science," edited by M. Green (Marcel Dekker, New York, 1969) Vol. 1.
84. C. TOMPKINS, in "The Solid-Gas Interface," edited by E. A. Flood (Marcel Dekker, New York, 1967) Chapt. 25.
85. S. MATSUSHIMA, Y. TERAOKA, N. MIURA and N. YAMAZOE, *Jpn. J. Phys.* **27** (1988) 1798.
86. N. YAMAZOE, Y. KUROKAWA and T. SEIYAMA, *Sensors and Actuators* **4** (1983) 283.
87. A. R. GONZALEZ-ELIPE, J. SORIA and G. MUNUERA, *J. Catal.* **76** (1982) 254.
88. N. YAMAMOTO, S. TONOMURA, T. MATSUOKA and H. TSUBOMURA, *J. Appl. Phys.* **52** (1981) 6227.
89. K. KIMOTO and S. R. MORRISON, *Z. Phys. Chem. N. F.* **108** (1977) 11.
90. K. D. SCHIERBAUM, U. K. KIRNER, J. F. GEIGER and W. GÖPEL, *Sensors and Actuators* B **4** (1991) 87.
91. N. YAMAZOE, Y. KUROKAWA and T. SEIYAMA, *ibid.* **4** (1983) 283.
92. CRANK, "The Mathematics of Diffusion," 2nd ed. (Oxford Science Publications, 1975) p. 334.
93. P. T. MOSELEY and B. C. TOFIELD, "Solid State Gas Sensors" (Adam Hilger, 1987) p. 103.
94. M. EGASHIRA, Y. SHIMIZU and Y. TAKAO, in Proc. Symp. on Chemical Sensor II, edited by M. Butler, A. Ricco and N. Yamazoe, Vol. 93-7 (The Electrochemcical Soc., NJ, 1993) p. 510.
95. W. GÖPEL and G. REINHARDT, "Sensors Update," Vol. 1 (VCH, Weinheim, 1996) p. 47.
96. X. VILANOVA, E. LIOVET, J. BREZMES, J. CALDERER and X. CORREIG, *Sensors and Actuators* B **48** (1998) 425.
97. N. KOMORI, S. SAKAI and K. KOMATSU, in Proc. Int. Meeting on Chem. Sensors, Fukuoka, Japan, edited by T. Seiyama, *et al*. (Kodansha and Elsevier, 1983) p. 57.
98. M. FLEISCHER, M. SETH, C.-D. KOHL and H. MEIXNER, *Sensors and Actuators* B **35/36** (1996) 297.
99. A. KATSUKI and K. FUKUI, *ibid*. B **52** (1998) 30.
100. M. FLEISCHER and H. MEIXNER, *ibid*. **52** (1998) 179.
101. C. O. PARK, S. A. AKBAR and J. HWANG, *Mater. Chem. Phys.* **75** (2002) 56.
102. P. DUTRONC, B. CARBONNE, F. MENIL and C. LUCAT, *Sensors and Actuators* B **6** (1992) 279.
103. U. WEIMAR and W. GÖPEL, *ibid*. B **26/27** (1995) 13.
104. U. HOEFER, K. STEINER and E. WAGNER, *ibid*. **26/27** (1995) 59.
105. M. BAUER, N. BARSAN, K. INGRISH, A. ZEPPENFELD, I. DENK, B. SCHUMAN, U. WEIMAR and W. GÖPEL, in Proc. European Microelectronic Conference, May 1997, Venice, Italy, p. 14.
106. N. BARSAN, M. S. BERBERICH and W. GÖPEL, *Fresenius J. Anal. Chem.* **365** (1999) 287.
107. K. IHOKURA and J. WATSON, "The Stannic Oxide Gas Sensor" (CRC Press, 1994) p. 149.
108. N. SAVAGE, B. CHWIEROTH, A. GINWALLA, B. R. PATTON, S. A. AKBAR and P. K. DUTTA, *Sensors and Actuators* B **79** (2001) 17.
109. NBS Special Publication 480-41.
110. T. TAKADA, *Sensors and Actuators* B **52** (1998) 45.
111. S. SEMANCIK and R. CAVICCHI, *Acc. Chem. Res.* **31** (1998) 279.
112. J. W. GARDNER and P. N. BARTLETT (eds.), Sensors and Sensory Systems for an Electronic Nose. NATO ASI Series E: Applied Science, Vol. 212 (Kluwer, Dordrecht, 1992).
113. L. CHAMBON, J. P. GERMAIN, A. PAULY, V. DEMARNE and A. GRISEL, *Sensors and Actuators* B **60** (2000) 138.
114. H.-K. HONG, H. W. SHIN, D. H YUN, S.-R. KIM, C.-H. KWON, K. LEE and T. MORIIZUMI, *ibid.* **35/36** (1996) 338.
115. M. FULKERSON, Ph.D. thesis, The Ohio State University, Columbus, OH, 2002.
116. M. FRANK, M. FULKERSON, B. PATTON and P. DUTTA, *Sensors and Actuators* **B87** (2002) 471.
117. C. CIOBANU, Y. LIU, Y. WANG and B. R. PATTON, *J. Electroceram.* **3** (1999) 15.
118. B. CHWIEROTH, B. R. PATTON and Y. WANG, *J. Electroceram.* **6** (2001) 27.